Locally ordered representation of 3D space in the entorhinal cortex

https://doi.org/10.1038/s41586-021-03783-x

Received: 8 January 2020

Accepted: 29 June 2021

Gily Ginosar[1], Johnatan Aljadeff[1,2], Yoram Burak[3,4], Haim Sompolinsky[3,4,5], Liora Las[1] & Nachum Ulanovsky[1]✉

As animals navigate on a two-dimensional surface, neurons in the medial entorhinal cortex (MEC) known as grid cells are activated when the animal passes through multiple locations (firing fields) arranged in a hexagonal lattice that tiles the locomotion surface[1]. However, although our world is three-dimensional, it is unclear how the MEC represents 3D space[2]. Here we recorded from MEC cells in freely flying bats and identified several classes of spatial neurons, including 3D border cells, 3D head-direction cells, and neurons with multiple 3D firing fields. Many of these multifield neurons were 3D grid cells, whose neighbouring fields were separated by a characteristic distance—forming a local order—but lacked any global lattice arrangement of the fields. Thus, whereas 2D grid cells form a global lattice—characterized by both local and global order—3D grid cells exhibited only local order, creating a locally ordered metric for space. We modelled grid cells as emerging from pairwise interactions between fields, which yielded a hexagonal lattice in 2D and local order in 3D, thereby describing both 2D and 3D grid cells using one unifying model. Together, these data and model illuminate the fundamental differences and similarities between neural codes for 3D and 2D space in the mammalian brain.

The world is three-dimensional, but little is known about how the mammalian cortex represents 3D space[2]. Here we studied 3D spatial coding in the medial entorhinal cortex (MEC) of a flying mammal: the Egyptian fruit bat. In rodents running on 2D surfaces, many MEC neurons exhibit multiple firing fields arranged in varying degrees of order[1,3,4]; the fields of the most ordered neurons—grid cells—are arranged in a hexagonal pattern to form a global 2D lattice[1]. Grid cells have been studied extensively in rodents navigating on horizontal, sloping, and vertical 2D surfaces[1,5–7], and 2D grid cells in bats during crawling have previously been found[8]. Here we identified 3D grid cells, which exhibited multiple 3D firing fields separated by a characteristic distance from nearby fields—a key property of 2D grid cells—thus exhibiting local spatial order. Unlike 2D grid cells, 3D grids did not exhibit hexagonality or any other global lattice structure. Thus, 3D grid cells displayed a locally ordered spatial code, rather than a globally ordered one as in 2D grids—constraining the possible mechanisms and functions of grid cells. We show that a simple principle from physics can elucidate the neural code for space across spatial dimensions. In addition, we identified 3D head-direction cells[9–11], as well as border cells[12,13] that encode the boundaries of 3D space. Together, these data elucidate the neural representation of 3D allocentric space in the mammalian cortex.

3D grids show local rather than global order

Grid cells recorded on 2D surfaces[1] exhibit: (1) roughly circular fields; (2) a hexagonal field arrangement; (3) fields that lie on the vertices of a lattice; (4) prominence of 60° angles; and (5) relatively fixed distances between neighbouring fields. For 3D grids, we hypothesized several possible field arrangements, ranging from highly ordered to random arrangements (Fig. 1a, b, Extended Data Fig. 1a, b). To record grid cells in 3D, we trained bats to fly in a large room ($5.8 \times 4.6 \times 2.7$ m) while we wirelessly recorded the activity of single neurons in MEC (Methods). To ensure that the bats would comprehensively explore 3D space, we placed 6–11 landing balls (feeding locations) near the walls at various heights (Fig. 1c). Bats flew large distances (1.7 ± 0.7 km per session; mean ± s.d.), creating dense 3D coverage of the room (Fig. 1d, e, Extended Data Fig. 1c, d). Despite our efforts, bats were unable to produce sufficient spatial coverage for us to record the same neurons in both 3D flight and 2D crawling, because of exhaustion, so we do not compare here the same neurons in 3D and 2D. We recorded from four bats 125 cells that met criteria of minimal session duration and number of spikes in-flight. Recordings were distributed roughly equally across the superficial and deep layers of MEC (Fig. 1f, Extended Data Fig. 2). Many cells had multiple 3D fields, firing when the bat passed through one of several restricted 3D locations (Fig. 2a, Extended Data Fig. 3a, d). The bats' flights were non-stereotypic, and firing fields were composed of multiple underlying flights in various directions (Fig. 1e bottom, Extended Data Figs. 4, 5). We focused on neurons that exhibited ten or more stable firing fields, which we call 'multifield cells' (66 of 125 neurons, 52.8%) (Fig. 2a–d, Extended Data Fig. 3c, d). These cells exhibited high 3D-map correlations for odd versus even minutes (Fig. 2e, median map correlation: $r = 0.84$).

---

[1]Department of Neurobiology, Weizmann Institute of Science, Rehovot, Israel. [2]Department of Bioengineering, Imperial College London, London, UK. [3]The Edmond and Lily Safra Center for Brain Sciences, The Hebrew University of Jerusalem, Jerusalem, Israel. [4]Racah Institute of Physics, The Hebrew University of Jerusalem, Jerusalem, Israel. [5]Center for Brain Science, Harvard University, Cambridge, MA, USA. ✉e-mail: nachum.ulanovsky@weizmann.ac.il

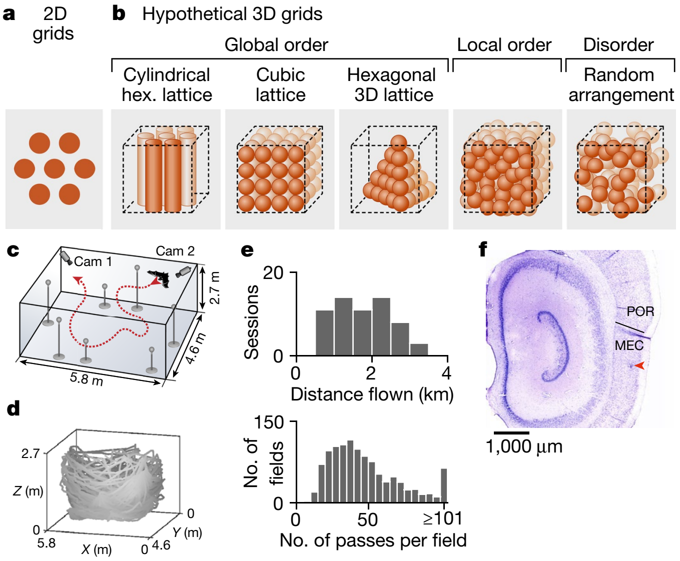

Fig. 1 | Experimental setup and behaviour. a, Cartoon of 2D grid pattern. **b**, Possible hypothetical arrangements of 3D grids. **c**, Experimental setup: bats flew freely in a 5.8 × 4.6 × 2.7-m room, foraging for food placed on 6–11 landing balls positioned at various heights near the walls. **d**, **e**, Behavioural coverage. **d**, Typical bat trajectory from one recording session. **e**, Top: distribution of distance flown per recording-session, for all sessions with valid neurons ($n = 61$ sessions; 4 bats). Bottom: distribution of number of passes per field, for all multifield neurons ($n = 1{,}113$ fields from 66 cells; showing passes with 3D distance ≤50 cm from field peaks; see Extended Data Fig. 4a for distance ≤30 cm). **f**, Example tetrode track in layer 3 of MEC; red arrowhead, recording location of cell 4 in Fig. 2a. POR, postrhinal cortex; black line, MEC–POR border.

We first examined individual field shapes and found that fields were roughly spherical, resembling the shape of hippocampal 3D place fields in bats[14], with no systematically vertically elongated fields[5] (Fig. 2b, Extended Data Fig. 3e). This argued against the presence of cylindrical fields (Fig. 1b, first model), and therefore we subsequently considered only models with roughly spherical fields.

Second, we sought to determine whether these cells exhibited globally ordered field arrangement, in particular a 3D hexagonal lattice. Optimal packing of spheres in 3D is achieved by two hexagonal lattices—face-centred cubic (FCC) and hexagonal close pack (HCP)[15] (Extended Data Fig. 6a)—both of which have been proposed as probable arrangements for 3D grid cells by several theoretical studies[16–18]. We exhaustively compared the field positions of each multifield cell to roughly three million FCC and HCP structures, systematically varying their seven free parameters (3 × shift, 3 × rotation, 1 × spacing), and identified the best-fitting lattice. To assess significance, we computed the fit error between the cell's 3D field arrangement and its best-fitting lattice, and compared it to the best-fit errors for 3D field arrangements derived from the cell's shuffled spikes (Extended Data Fig. 6b). Fewer cells than expected by chance had significant FCC fit (3 of 66 cells; binomial test for population-wide significance (with expected $P_0 = 0.05$): $P = 0.64$); and no cells (0 of 66) had significant HCP fit (Fig. 2c, f). Furthermore, only 0.54% of all fields (6 of 1,113 fields across the 66 neurons) were classified as part of a local FCC or local HCP crystalline domain (Methods). We therefore conclude that the 3D multifield cells exhibited neither global hexagonal lattices, nor local hexagonal lattice domains. We further investigated whether fields were arranged in any lattice, including non-hexagonal lattices. We computed the local angles between triplets of neighbouring fields, in search of overrepresentation of any angles (for example, 90° for a cubic lattice). We found no significant bias for any angle (Extended Data Fig. 6c; Kolmogorov–Smirnov test compared to shuffle, $P = 0.80$), which suggested that fields did not exhibit local orientational order and did not form any global lattice in 3D (ruling out the second and third options in Fig. 1b).

Third, we tested whether a basic property of 2D grids—the characteristic distance between neighbouring fields—is conserved in 3D. We computed the local distances between each field and its three nearest neighbours (Extended Data Fig. 6d, e). As in 2D grids, many cells exhibited a characteristic distance between neighbouring fields, indicated by a narrow distribution of distances (Fig. 2d, three leftmost neurons). To quantify the variability in distances, we calculated for each cell the coefficient of variation (CV = s.d./mean) of the distribution of nearest-neighbour distances; significance was determined by comparing the CV to the CVs for shuffled data from the same cell. For robustness, we used two types of shuffling: (1) spike shuffling: a random rigid circular shift of spike times, for which we used only shuffles with the same number of fields as in the real neuron (±3 fields); and (2) field shuffling: a random spatial shift of fields within the volume visited by the bat. With the spike-shuffling method, 21% (14 of 66) of the multifield cells showed a significantly narrow distribution of distances between neighbouring fields (Fig. 2d, f; binomial test (with expected $P_0 = 0.05$): $P = 4 \times 10^{-6}$). With the field-shuffling method, 30% (20 of 66) of the cells exhibited a significantly narrow distribution of distances (Fig. 2f, rightmost bar; binomial test: $P = 4 \times 10^{-11}$). Notably, all of the cells that were identified by spike shuffling were also identified by field shuffling, highlighting the robustness of the result. Thus, the fields of these cells were locally ordered, with a characteristic distance between neighbouring fields—ruling out randomly arranged fields (Fig. 1b, rightmost option). These firing patterns conserved three basic properties of 2D grids—multiple fields with isotropic field shapes and a characteristic distance between neighbouring fields—and therefore we considered these locally ordered neurons to be 3D grid cells (Fig. 2a–d, three leftmost neurons). The lack of global order could not be explained by distortions of globally ordered 3D structures (Fig. 2g, Extended Data Fig. 7) or by proximity to room borders (Extended Data Fig. 6g, h). Together, our data show that bat MEC contained about 50% cells with multiple roughly spherical fields, 20–30% of which were 3D grid cells that exhibited local order (local distances) but without a global lattice or hexagonal symmetry (consistent with Fig. 1b, fourth option).

The fields of grid cells and non-grid multifield cells covered the room uniformly (Fig. 3a; cells classified by spike shuffling). Furthermore, both 3D grid cells and non-grid multifield cells exhibited a gradient of increasing inter-field distances along the dorsoventral anatomical axis of MEC, as seen in 2D grid cells in rodents and bats[1,8] (Fig. 3b left, Extended Data Fig. 8). Correspondingly, the number of fields per cell decreased along the dorsoventral axis (Fig. 3b right). The distribution of CV values showed a unimodal continuum across 3D grid cells and non-grid multifield cells (Fig. 3c). There were no significant differences between grid cells and non-grid multifield cells in their field size, number of fields, or inter-field distances (Fig. 3d–f; *t*-tests, $P \geq 0.15$ for all comparisons). These results—and in particular the anatomical gradient observed in both grid cells and non-grid multifield cells (Fig. 3b), along with the unimodal CV distribution (Fig. 3c)—suggest that 3D grid cells and non-grid multifield cells form a continuum of local order, and are not two separate populations of cells.

3D properties of other MEC cell types

Next, we examined whether any of the other spatial cell types known from 2D representations in rodent MEC[10,12,13] could be found in 3D representations. Indeed, of the recorded neurons, 40.8% (51 of 125 cells) were significantly tuned to azimuthal head direction, 14.4% were significantly tuned to head pitch (18 of 125 cells), and a minority were tuned conjunctively to azimuth × pitch[11] (8 cells; 15.7% of azimuth cells, and 44.4% of pitch cells; Fig. 4a). As in rodents[19], azimuthal head-direction cells were more abundant in deep than in superficial layers of MEC (68.9% of all neurons recorded in layers 5–6 were azimuthal head-direction cells,

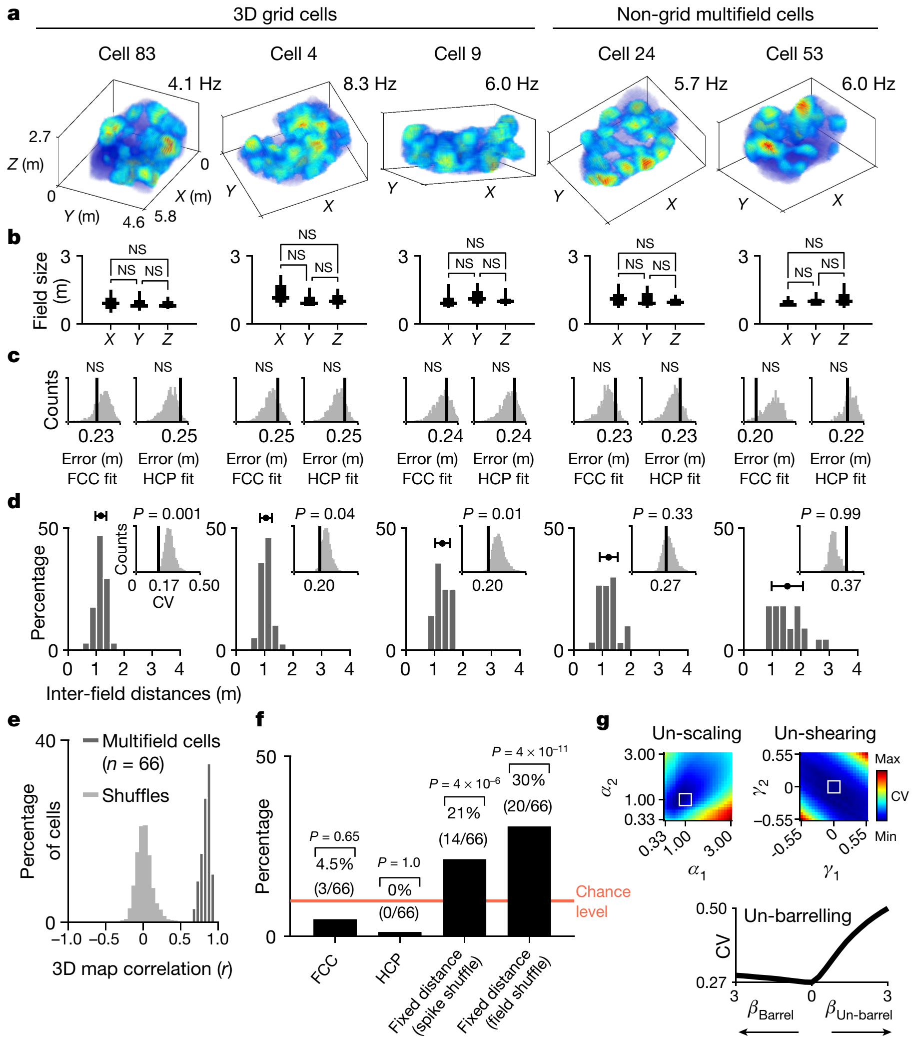

Fig. 2 | 3D grid cells in flying bats exhibit fixed local distances but no global lattice. a–d, Five example neurons with at least ten firing fields, and their characterization (columns: different neurons). **a**, 3D firing-rate maps; colour-coded from zero (blue) to maximal firing rate (red; value indicated above plot). **b**, Box plots depicting field-sizes for each neuron along the *x*, *y* and *z* room axes. Horizontal line, median across fields; box limits, 25th to 75th percentiles; whiskers, 10th to 90th percentiles. NS, not significant (Wilcoxon rank-sum tests comparing field-sizes in *x* versus *y*, *y* versus *z* and *x* versus *z*, Bonferroni-corrected for three pairwise comparisons). $n_{\text{fields}} = 20, 20, 17, 16, 12$ from left to right. **c**, Fits to hexagonal lattices—FCC (left) and HCP (right): black line, best-fit error for data; histogram, distribution of best-fit errors for shuffles. **d**, Distribution of distances between each field and its three nearest neighbours; horizontal bar, mean ± s.d. Inset: black line, CV of the cell's distance distribution (value indicated below); histogram, distribution of CVs for spike shuffles (*P* value of data indicated). **e**, Dark grey, distribution of Pearson correlations between 3D firing-rate maps for odd versus even minutes ($n = 66$ multifield cells). Light grey, cell shuffling (odd versus even minutes for different cells). **f**, Population analysis. Two rightmost bars, percentage of 3D grid cells exhibiting significantly fixed distances between neighbouring fields (21% are 3D grid cells using spike shuffling: binomial test, $P = 4 \times 10^{-6}$; and 30% are 3D grid cells using field shuffling: binomial test, $P = 4 \times 10^{-11}$). Two leftmost bars, fits to FCC and HCP; a non-significant number of neurons exhibited FCC or HCP lattices compared to shuffle (FCC: 3 of 66 cells, binomial test: $P = 0.65$; HCP: 0 of 66 cells, binomial test: $P = 1.0$). Red line, population-wide chance level (binomial test). **g**, 'Un-distortions' (un-scaling, un-shearing and un-barrelling) of field arrangements of recorded cells, and the corresponding CV values. White squares in the top graphs and $\beta = 0$ in the bottom graph correspond to the original experimental data without un-distortions. Full analysis in Extended Data Fig. 7.

versus 34.1% in layers 2–3). Some recorded cells were conjunctive 3D grid × head-direction cells, or multifield × head-direction cells (for example, cell 83: Figs. 2a, 4a).

In addition, we found border cells[12,13] in 3D—the first such report, to our knowledge, in any species. Eight per cent of all recorded neurons were either 2D or 1D border cells embedded in 3D space (Fig. 4b, Extended Data Fig. 9a–c; 10 of 125 cells, identified using 99% shuffling threshold on an elongation index; binomial test (with expected $P_0 = 0.01$): $P = 6 \times 10^{-7}$; 8 of 10 were 2D border cells and 2 of 10 were 1D border cells). The prevalence of border cells in bat MEC was similar to that in rats[12]. Thus, along with 3D grid cells, bat MEC contains other spatially tuned cells, similar to those reported in rodent MEC for 2D representations—but here encoding 3D space (Fig. 4c, Extended Data Fig. 9d).

A unifying model for 3D and 2D firing

Finally, we set out to phenomenologically model the geometry of 3D spatial representation in MEC: local order without a global lattice (Fig. 5, Extended Data Figs. 10–14). Inspired by statistical physics of multiple particle systems, we regarded firing fields of multifield neurons as 'particles' that are subject to distance-dependent pairwise

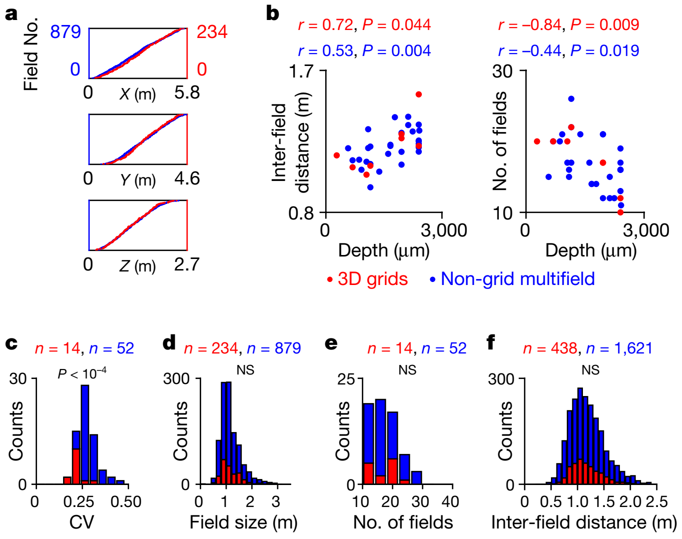

Fig. 3 | Properties of 3D grid cells and non-grid multifield cells. a, Room coverage by fields of 3D grid cells (red) and non-grid multifield cells (blue; cell classification based on spike shuffling). Shown are field positions (pooled and sorted; number of fields indicated), plotted separately for the *x*, *y* and *z* dimensions. **b**, Mean inter-field distance (left) and number of fields (right) plotted against the dorsoventral recording depth in MEC; only cells from tetrode tracks with reliable estimates of recording depth are shown. Pearson correlations are indicated separately for grid cells (red) and non-grid multifield cells (blue). **c**–**f**, Characterizing 3D grid cells (red) and non-grid multifield cells (blue). Distributions of CV (**c**), field size (**d**), number of fields per neuron (**e**) and inter-field distance (**f**) are shown; *n* indicated; *t*-tests compared grid cells to non-grid multifield cells ($t = 4.38, 2\times10^{-3}, 0.13, 1.42$; $P = 4\times10^{-5}, 0.99, 0.89, 0.15$ for **c**–**f**, respectively).

interactions—repulsion of close fields and attraction of more distant ones, creating an equilibrium distance between fields. Individual fields were allowed to move under the influence of these interactions, consistent with reports of individual grid fields moving in 2D[20–22]. We used the classical Lennard–Jones potential, in which a distance parameter r_0 controls the equilibrium distance between neighbouring fields (Fig. 5a). A noise parameter (represented by the system's 'temperature', T) controls the deviation of fields from equilibrium position. For each recorded cell, we fitted the two parameters, r_0 and T, to yield values of CV and mean inter-field distance that matched those of the cell. We focused on the ordered roughly half of the multifield population, neurons with CV < 0.25 (29 of 66 neurons; for simulations of the less ordered neurons with CV > 0.25, see Extended Data Fig. 10d, e).

To evaluate how well the model describes the data, we used the radial distribution function (RDF), which portrays the distribution of distances between all possible field pairs. We computed the RDF from distances pooled over all the 29 locally ordered recorded neurons (Fig. 5b, black). In addition, we computed the RDFs for simulations of the Lennard–Jones model, and for three alternative models: (1) random Poisson model, in which the same number of fields was randomly distributed throughout the space the bat explored; and two biologically plausible versions of a perfect 3D lattice: (2) jittered FCC model, and (3) jittered HCP model (Fig. 5b, Extended Data Fig. 12a). A distance index was computed between the data RDF and each of the model RDFs, and it showed that the data were fitted much better by the Lennard–Jones model than by the alternative models (Fig. 5c, *t*-test: $P < 10^{-300}$ in all cases). Similar good fits were obtained using two additional pairwise-interaction potentials of short-range repulsion and long-range attraction between firing fields (Extended Data Fig. 10b, c), which suggests robustness to the exact shape of the potential. Thus, diverse pairwise-interaction potentials successfully described our experimental finding of local, but not global, order in 3D.

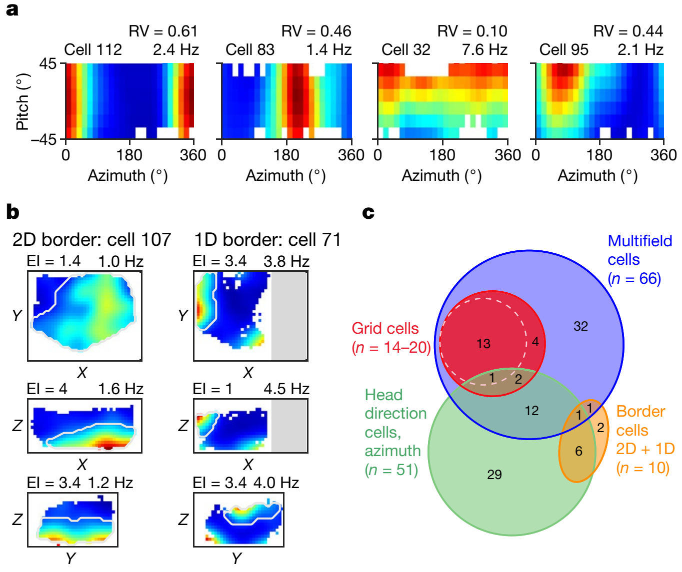

Fig. 4 | 3D head-direction cells and 3D border cells in bat MEC. a, Examples of head-direction cells, showing firing-rate maps as a function of azimuth × pitch; firing rate is colour-coded from zero (blue) to maximal firing rate (red, value indicated). RV, Rayleigh vector length of azimuth modulation. Cell 83 is a grid cell (Fig. 2a, leftmost neuron). **b**, Examples of border cells. Left, cell active along a 2D planar border of space (the floor). Right, cell active along a 1D border of space (the wall edge). Top, top view of room (*xy*); middle and bottom panels, side views (*xz* and *yz*). Firing-rate maps colour-coded from zero (blue) to the maximal firing rate across the cell's three views (red). White lines, detected firing fields (enlarged by one bin for display); elongation index (EI) and peak firing rate are indicated. Grey rectangle, room area made inaccessible to bat 4. **c**, Population summary of functional cell classes in bat MEC. Red circle, significant grid cells using field shuffling; dashed circle within it, subpopulation of significant grid cells using spike shuffling.

We next examined whether our model could also capture properties of 2D grids, and therefore used the Lennard–Jones model to simulate 2D arenas. To compare 2D and 3D simulations using the same equations, we conducted the 2D simulations in a 10-cm-high room, which was effectively 2D but still retained three dimensions. The comparison was made using the RDF because it captures order at any dimensionality, whereas the classical 'gridness score' is defined only in 2D[10]. We observed a prominent second peak in the RDF of the 2D simulations, but not in the 3D simulations (Fig. 5d). Whereas an RDF peak at the characteristic distance indicates local order, a second peak indicates longer-range order, as in lattices. We therefore defined a 'regularity index' that quantifies the RDF's second-peak (Extended Data Fig. 11a), and found high regularity values in 2D simulations but not 3D simulations—indicating long-range order in 2D but not in 3D (Extended Data Fig. 13). Furthermore, in the 2D simulations, fields were often arranged in nearly perfect hexagons with high hexagonal gridness scores (Fig. 5d bottom right, Extended Data Fig. 11c, d). Such hexagonal 2D structures have been shown to emerge in 2D simulations of a modified Lennard–Jones potential[23], but here we found that introducing noise (temperature T) was crucial for describing the local but not global structure of the 3D data, while maintaining the global hexagonal structure in 2D. Notably, our results were robust for a broad range of values of the simulation parameters (temperature T, interaction distance r_0, room size, number of fields, and field density: Extended Data Figs. 12–14). In addition, the gridness scores of simulated 2D grids decreased in larger rooms, suggesting that the crystallization of hexagonal grids in 2D is affected by the ratio between arena size and grid scale (Extended Data Fig. 11e; we maintained a fixed effective density of fields, ρ_{eff} (see Extended Data Fig. 11b for definition of ρ_{eff})). We therefore predict that

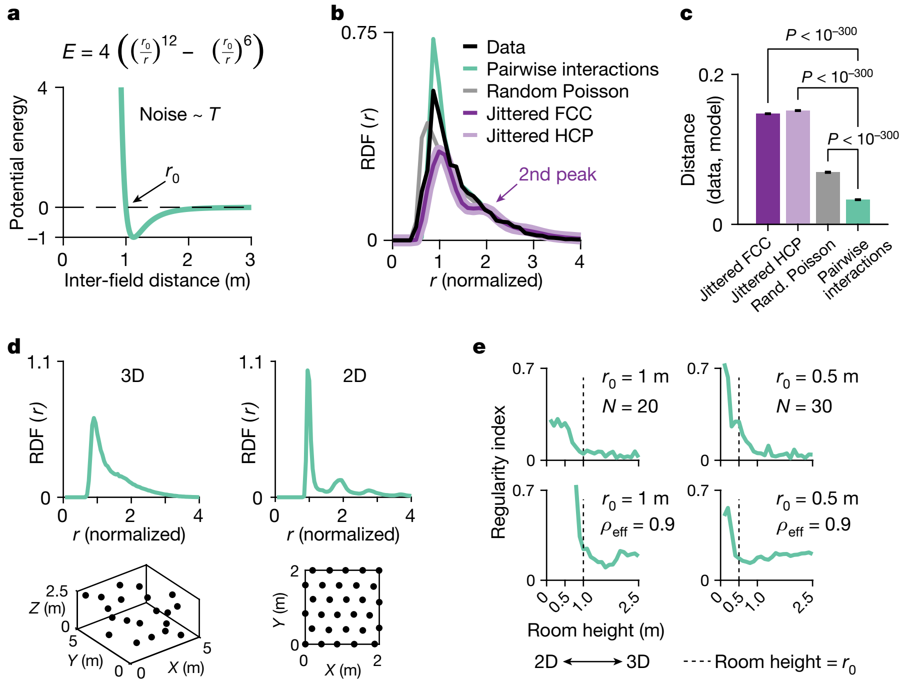

Fig. 5 | A single model describes both grid-cell hexagonality in 2D and the local-but-not-global order in 3D. a, Lennard–Jones potential: r_0, distance parameter; here $r_0 = 1$ m (note the equilibrium position at potential minimum is $1.12 \times r_0$, which matches the typical inter-field distance of 3D grid cells in our data). T, temperature: controls field deviations from equilibrium position. **b**, **c**, Simulations matched to recorded cells with CV < 0.25 ($n = 29$), pooled across cells. **b**, RDFs for data and four models. Model RDFs show mean of 1,000 simulations. **c**, Distances between RDF of data and 1,000 RDFs of each model (mean ± s.e.m.). **d**, Simulations of pairwise-interactions model in 3D (left) and 2D (right), showing RDF (top; mean of 500 simulations) and simulation examples (bottom). Simulated using typical parameters from experimental data (3D: room size, 5 × 5 × 2.5 m; 20 fields; model parameters, $\log_{10}T = 0.5$, $r_0 = 1$ m (based on our 3D grid cells); 2D: room size, 2 × 2 m; 30 fields; model parameters, $\log_{10}T = 0.5$, $r_0 = 0.5$ m (based on typical 2D grid cells from rats[24])). **e**, Regularity index as a function of room height, from effectively 2D (0.1 m room height) to a full 3D room (2.5 m room height). Computed for fixed number of fields N (top) or fixed effective density ρ_{eff} (bottom), using r_0 corresponding to 3D data (left) or 2D data (right). Note the drop in regularity when going from 2D to 3D, regardless of which variable is held fixed.

in rat or bat grid cells recorded in very large 2D boxes, neurons with a small-scale 2D grid compared to the room size will exhibit disrupted hexagonality, whereas large-scale 2D grids will be hexagonal.

Finally, we explored the regularity of field arrangements throughout the transition from 2D to 3D arenas. We conducted simulations for various room heights, incrementally changing the height from effectively 2D to 3D while keeping constant either the number of fields (Fig. 5e top) or the effective field density ρ_{eff} (Fig. 5e bottom, Extended Data Fig. 11g). The distance-parameter r_0 in these simulations corresponded either to our 3D data ($r_0 = 1$ m) or to published 2D data[24] ($r_0 = 0.5$ m). All cases showed a clear transition in regularity from long-range global order in 2D to local order in 3D: this transition occurred approximately at a room height that allowed more than one layer of fields (Fig. 5e). Together, the experimental data and modelling suggest that the grid pattern may emerge from pairwise interactions between fields—creating a hexagonal global lattice in 2D, but only local order in 3D. Furthermore, this suggests that the 2D grids seen in rodents and bats are not a consequence of a planar cut through a 3D grid, but result from effective pairwise interactions between fields that are restricted to a 2D surface.

Discussion

We recorded MEC cells from bats flying volumetrically in 3D space, and found a variety of spatially tuned neurons, including 3D head-direction cells, 3D border cells, and 3D grid cells, which exhibited characteristic distances between fields (that is, 3D local order), but no 3D lattice arrangement. This finding stands in notable contrast to the global hexagonal lattices of 2D grid cells, and to theoretical models of 3D grid cells that have predicted hexagonal lattices in 3D[16–18]. We proposed a model based on pairwise interactions between firing fields, which provided a unified description for both 3D and 2D grid cells.

We considered the mechanistic implications of our results. While the pairwise interactions model is phenomenological, such pairwise interactions between fields may arise mechanistically from plasticity in feedforward synaptic inputs to 3D grid cells[25]. Furthermore, we hypothesize that our results might be compatible with the framework of continuous attractor models of grid cells[26,27]; however, existing attractor models would need to be substantially modified to reconcile them with our findings of local but not global order in 3D (for details on possible mechanistic models, see 'Additional discussion' in Methods).

Finally, our results have important implications for the possible functional role of grid cells. Classical theories on the function of 2D grid cells relied on the fundamental assumption that grid cell firing patterns are periodic[27–30]. Moreover, suggestions that grid cells are involved in geometric computations such as goal-directed navigation[27,28,30] were motivated by the highly geometric, periodic representation of 2D space by grid cells. Given our findings on the absence of global periodicity in 3D, it seems less plausible that 3D grid cells are involved in general-purpose geometric computations, particularly during large-scale 3D navigation. We therefore suggest that global spatial periodicity is not central to the function of grid cells—which calls for the development of new models to describe the contribution of grid cells to spatial navigation in both 2D and 3D environments.

Online content

Any methods, additional references, Nature Research reporting summaries, source data, extended data, supplementary information, acknowledgements, peer review information; details of author contributions and competing interests; and statements of data and code availability are available at https://doi.org/10.1038/s41586-021-03783-x.

1. Hafting, T., Fyhn, M., Molden, S., Moser, M.-B. & Moser, E. I. Microstructure of a spatial map in the entorhinal cortex. *Nature* **436**, 801–806 (2005).
2. Finkelstein, A., Las, L. & Ulanovsky, N. 3-D maps and compasses in the brain. *Annu. Rev. Neurosci*. **39**, 171–196 (2016).
3. Krupic, J., Burgess, N. & O'Keefe, J. Neural representations of location composed of spatially periodic bands. *Science* **337**, 853–857 (2012).
4. Stensola, T., Stensola, H., Moser, M.-B. & Moser, E. I. Shearing-induced asymmetry in entorhinal grid cells. *Nature* **518**, 207–212 (2015).
5. Hayman, R., Verriotis, M. A., Jovalekic, A., Fenton, A. A. & Jeffery, K. J. Anisotropic encoding of three-dimensional space by place cells and grid cells. *Nat. Neurosci*. **14**, 1182–1188 (2011).
6. Hayman, R. M., Casali, G., Wilson, J. J. & Jeffery, K. J. Grid cells on steeply sloping terrain: evidence for planar rather than volumetric encoding. *Front. Psychol*. **6**, 925 (2015).
7. Casali, G., Bush, D. & Jeffery, K. Altered neural odometry in the vertical dimension. *Proc. Natl Acad. Sci. USA* **116**, 4631–4636 (2019).
8. Yartsev, M. M., Witter, M. P. & Ulanovsky, N. Grid cells without theta oscillations in the entorhinal cortex of bats. *Nature* **479**, 103–107 (2011).
9. Taube, J. S., Muller, R. U. & Ranck, J. B. Jr Head-direction cells recorded from the postsubiculum in freely moving rats. I. Description and quantitative analysis. *J. Neurosci*. **10**, 420–435 (1990).
10. Sargolini, F. et al. Conjunctive representation of position, direction, and velocity in entorhinal cortex. *Science* **312**, 758–762 (2006).
11. Finkelstein, A. et al. Three-dimensional head-direction coding in the bat brain. *Nature* **517**, 159–164 (2015).
12. Solstad, T., Boccara, C. N., Kropff, E., Moser, M.-B. & Moser, E. I. Representation of geometric borders in the entorhinal cortex. *Science* **322**, 1865–1868 (2008).
13. Savelli, F., Yoganarasimha, D. & Knierim, J. J. Influence of boundary removal on the spatial representations of the medial entorhinal cortex. *Hippocampus* **18**, 1270–1282 (2008).
14. Yartsev, M. M. & Ulanovsky, N. Representation of three-dimensional space in the hippocampus of flying bats. *Science* **340**, 367–372 (2013).
15. Hales, T. C. A proof of the Kepler conjecture. *Ann. Math*. **162**, 1065–1185 (2005).
16. Stella, F. & Treves, A. The self-organization of grid cells in 3D. *eLife* **4**, e05913 (2015).
17. Mathis, A., Stemmler, M. B. & Herz, A. V. M. Probable nature of higher-dimensional symmetries underlying mammalian grid-cell activity patterns. *eLife* **4**, e05979 (2015).
18. Horiuchi, T. K. & Moss, C. F. Grid cells in 3-D: reconciling data and models. *Hippocampus* **25**, 1489–1500 (2015).
19. Boccara, C. N. et al. Grid cells in pre- and parasubiculum. *Nat. Neurosci*. **13**, 987–994 (2010).
20. Krupic, J., Bauza, M., Burton, S. & O'Keefe, J. Local transformations of the hippocampal cognitive map. *Science* **359**, 1143–1146 (2018).
21. Boccara, C. N., Nardin, M., Stella, F., O'Neill, J. & Csicsvari, J. The entorhinal cognitive map is attracted to goals. *Science* **363**, 1443–1447 (2019).
22. Sanguinetti-Scheck, J. I. & Brecht, M. Home, head direction stability, and grid cell distortion. *J. Neurophysiol*. **123**, 1392–1406 (2020).
23. Krupic, J., Bauza, M., Burton, S., Lever, C. & O'Keefe, J. How environment geometry affects grid cell symmetry and what we can learn from it. *Phil. Trans. R. Soc. Lond. B* **369**, 20130188 (2013).
24. Stensola, H. et al. The entorhinal grid map is discretized. *Nature* **492**, 72–78 (2012).
25. Kropff, E. & Treves, A. The emergence of grid cells: intelligent design or just adaptation? *Hippocampus* **18**, 1256–1269 (2008).
26. Burak, Y. & Fiete, I. R. Accurate path integration in continuous attractor network models of grid cells. *PLoS Comput. Biol*. **5**, e1000291 (2009).
27. McNaughton, B. L., Battaglia, F. P., Jensen, O., Moser, E. I. & Moser, M.-B. Path integration and the neural basis of the 'cognitive map'. *Nat. Rev. Neurosci*. **7**, 663–678 (2006).
28. Fiete, I. R., Burak, Y. & Brookings, T. What grid cells convey about rat location. *J. Neurosci*. **28**, 6858–6871 (2008).
29. Mathis, A., Herz, A. V. M. & Stemmler, M. B. Resolution of nested neuronal representations can be exponential in the number of neurons. *Phys. Rev. Lett*. **109**, 018103 (2012).
30. Stemmler, M., Mathis, A. & Herz, A. V. M. Connecting multiple spatial scales to decode the population activity of grid cells. *Sci. Adv*. **1**, e1500816 (2015).

Methods

Subjects and behavioural setup

Four adult male Egyptian fruit bats (*Rousettus aegyptiacus*, weight 160–173 g) were included in this work. No randomization or blinding was applied in this study. Sample size was not pre-determined; the number of animals is standard for studies in this research field. The bats were caught as adults in the wild (in Israel). Prior to the start of experiments, all bats were housed for several months in a large vivarium: a 5.3 × 5.0 × 2.9-m colony room with many enrichment items, where the bats flew extensively in 3D. Bats were maintained on a 12 h–12 h reversed light–dark cycle, both in the colony room and during experiments; all experimental recordings were conducted during the dark phase (the active period of the bats).

Bats were trained to fly in a large flight room (5.8 × 4.6 × 2.7 m). The bats covered extensive distances in each session, flying on average 1.7 ± 0.7 km per session (mean ± s.d.; Fig. 1e top, Extended Data Fig. 1d). Three of the bats were trained to land on 6–11 landing balls that were scattered around the periphery of the room (Fig. 1c). The balls had a 12-cm diameter and they were mounted on poles at various heights, from 60 to 200 cm. The diversity of heights encouraged the bats to cover as much of the room's volume as possible, and in particular to span well the *z* dimension of the room. The ball setup was re-arranged every few days, to create a new configuration of balls in the room. A fourth bat was not introduced to landing balls and instead was trained to land on the felt-covered walls of the room, at various heights. The setup used with this bat was a smaller version of the flight room: a see-through wall (nylon mesh) was constructed perpendicular to the long wall, creating a smaller room (3.9 × 4.6 × 2.7 m). Small pieces of fruit were randomly distributed either on the landing-balls (for the three bats trained to land on them) or on the walls (for the fourth bat that was not introduced to landing balls). Experiments were done under dim light (illuminance: 3 lux). Each recording session began and ended with a 5-min sleep session, during which the bat was placed inside the flight room in a small cage. These sleep sessions allowed us later to verify that neurons were recorded stably throughout the entire behavioural session, including the pre-test and post-test sleep sessions. The flight session in between these two sleep sessions typically lasted 50–90 min. All experimental procedures were approved by the Institutional Animal Care and Use Committee of the Weizmann Institute of Science.

Surgery and recording techniques

When a bat reached a sufficient level of training, it was implanted in the right hemisphere with a four-tetrode microdrive (weight 2.1 g; Neuralynx), loaded with four tetrodes, where each tetrode was created by winding together four strands of insulated wire (17.8 μm diameter platinum-iridium wire) as described previously[8,11,14,31,32]. Tetrodes were gold-plated to reduce wire impedance to between 0.3 and 0.7 MΩ (at 1 kHz). The microdrive was then implanted 4.5 mm lateral to the midline and 0.3–0.7 mm anterior to the transverse sinus that runs between the posterior part of the cortex and the cerebellum. The microdrive was angled 15° anteriorally in the sagittal plane and 19° laterally in the coronal plane, to allow the tetrodes to reach MEC and yield long recording tracks along the MEC layers (Extended Data Fig. 2). Surgical procedures were similar to those described previously[8,11,14,31,32]. We used an injectable anaesthesia cocktail composed of Medetomidine 0.25 mg/kg, Midazolam 2.5 mg/kg and Fentanyl 0.025 mg/kg, and subsequently added additional injections as needed, based on monitoring the bat's breathing and heart rate. The craniotomy was sealed with an inert elastomer (Kwik-Sil or Kwik-Cast). A ground screw was implanted in the frontal plate, and multiple bone screws were attached to the skull using an adhesive (Super-Bond), and were subsequently covered by dental acrylic, to hold the microdrive stably in place. Following surgery, the tetrodes were lowered 1.6–3.2 mm on the day of the surgery. For each bat, one tetrode was left in an electrically quiet zone and served as a reference, and the remaining three tetrodes served as recording probes. During recordings, each tetrode was lowered individually in small steps every day. A 16-channel wireless neural-recording device ('neural logger'; Deuteron Technologies, weighing 7.2 g, including electronics, battery, and protector) was attached to an Omnetics connector on the microdrive. Signals from all 16 channels of the 4 tetrodes were amplified (×200) and bandpass filtered (300–7,000 Hz), and were then sampled continuously at 29.3 kHz per channel, and stored on-board the neural logger. During subsequent processing, the neural recording was further filtered between 600 and 6,000 Hz for spikes, and then 1-ms spike waveforms were extracted using a voltage threshold.

Spike sorting and inclusion criteria

All spike-sorting procedures were identical to those described previously[8,11,14,31–33]. Spike waveforms were sorted on the basis of their relative energies and amplitudes on different channels of each tetrode (SpikeSort3D; Neuralynx). Data from all sessions—the behavioural session and the two sleep sessions—were spike-sorted together. Well-isolated clusters of spikes were manually selected, and a refractory period (<2 ms) in the interspike interval histogram was verified. We retained for further analysis only neurons that met the following inclusion criteria: (i) were stably isolated throughout all the sessions, including the pre and post sleep sessions; (ii) emitted more than 250 spikes in-flight (a large number of spikes is important for obtaining reliable 3D tuning in our large flight-room); (iii) were recorded in a behavioural session that lasted at least 45 min (median duration was 64 min); (iv) the bat spent at least 200 s in flight (median time in-flight was 483 s); (v) we excluded putative interneurons (mean firing rate >5 Hz). A total of 125 well-isolated, stable cells, which met all these criteria, were recorded across all the different layers of MEC (as was later confirmed by histology).

Video tracking

The position of the bat was tracked by two cameras located at two of the upper corners of the flight room. The cameras were connected to a video-tracker system (Neuralynx), which tracked the position of bright omnidirectional light-emitting diodes (LEDs), mounted on the bat's head. The video data were sampled at a 25-Hz rate. The 3D position of the bat was then reconstructed using the direct linear transform algorithm applied to data from both cameras, which yielded a 12-mm spatial accuracy[14,34]. The video data were synchronized with the neural recordings (neural logger) via a pseudo-random sequence of TTL pulses that was generated by the neural logger system and was recorded on the Neuralynx system: this yielded a temporal synchronization better than 1 ms.

Computing firing-rate maps

All the behavioural and neural data in this study were analysed using custom code written in Matlab. Firing-rate maps were constructed using flight epochs. A flight epoch was defined as a continuous epoch with flight-speed >120 cm/s. To prevent stationary data from contaminating our flight data, we omitted a buffer of ~1 s at the beginning and end of each flight. The room was then divided into 3D voxels of 10 × 10 × 10 cm. We used a conservative version of the adaptive smoothing previously described[14] (similar to adaptive smoothing used in rats[35,36]), as follows. Voxels with less than 1 s of behavioural data were pooled together with the closest voxels around them, creating a 3 × 3 × 3-voxel volume. The voxel in the centre of this volume was assigned the pooled time spent and pooled spike count over this volume. This procedure was repeated iteratively until either the minimum time spent of 1 s was reached, or the effective voxel size reached 7 × 7 × 7 voxels (30 cm effective radius), at which point we stopped. No further smoothing was applied to the data. Voxels in which the bat spent <1 s after enlargement to the maximal size (7 × 7 × 7 voxels) were excluded from the analysis and from the 3D firing-rate map, and were coloured white. Original voxels (of size 10 × 10 × 10 cm) that were >30 cm away from actual flight trajectories of the bat were also coloured white and were excluded from analysis. We then computed the firing-rate maps by dividing the smoothed spike-count map by the smoothed time-spent map. For all the 3D firing-rate maps, the colour scale ranged from zero (blue) to maximal firing rate (red). To test the stability of the firing-rate maps, we divided the data for each 3D firing-rate map into two parts: odd and even minutes in-flight. A separate firing-rate map was computed for each of the two halves of the data, and the Pearson correlation between the two maps was calculated (Fig. 2e, dark grey); for comparison we used the cell-shuffling method, wherein we computed the Pearson correlation between the firing-rate map created from the odd minutes of cell i, versus the map made from the even minutes of cell j, for all the cell-pairs i, j where $i \neq j$ (Fig. 2e, light grey).

Field detection

To examine cells with fields, we considered only 'patchy' cells, as quantified by the firing rate distribution across voxels: (i) the coefficient of variation of voxels' firing rates was >0.5, thereby excluding neurons with firing-rate maps that had low variance (smooth maps); and (ii) the skewness of voxels' firing-rates was <5 times the mean firing rate, thereby excluding maps with large outliers. These criteria left 103 out of the 125 cells for further consideration and field detection. Field detection was then done in two stages. (i) We identified the approximate position of the field's peak by local maximum detection. To this end, we smoothed the map using a 3D Gaussian to allow robust peak detection. This extra smoothing was used only for gross peak detection, and was not applied to the displayed firing-rate maps (Fig. 2a) or for any other analyses. We then applied to the smoothed map an algorithm for detecting local maxima in 3D matrices (MinimaMaxima3D.m, Matlab Central) to find local peaks (fields). In cases of peaks less than 0.6 m apart, the peak with the higher firing rate was chosen. (ii) Subsequently, we assessed the field's centre-of-mass by fitting a 3D Gaussian to the local region surrounding the peak; this fitting was done on the regular (un-smoothed) 3D firing map. Peak position was then taken as the fitted Gaussian's mean. This two-stage procedure yielded a more robust estimate of the centre location of the field, as compared to using standard peak detection, because our use of centre-of-mass weighing is relatively insensitive to small overlying noise (we note, though, that the differences between the two estimates were very small, typically just a few centimetres).

For field analysis, we considered only peaks with firing rates larger than the mean firing rate of the entire map. To ensure stability and reliability of individual fields, peaks were required to pass three criteria: (i) have a firing-rate higher than the 75th percentile of shuffled data at the same location (same exact voxel) as the peak – that is, higher than the firing rates across 75% out of 2,000 spike-shuffled maps at that location. This threshold eliminated fields that occurred due to low time spent, which were present across many shuffles, but it allowed us to identify fields in cells with a high baseline firing rate. See Extended Data Fig. 3b for the distribution of shuffle percentiles across all the fields. First, this figure shows that the 75% threshold was set at a natural kink in the distribution; and second, it demonstrates that for the large majority of fields, their peak was in fact much higher than 75% of the shuffles. (ii) Have at least five different visits of the bat in the vicinity of the field peak (less than 30 cm from the peak), with (iii) at least two of these visits with spikes. We note that the large majority of fields had many more than five flights within <30 cm—with a mean of 21 flights per field—so that the fields were based on very dense behavioural coverage (see also Extended Data Figs. 1c, 4a, c). We considered for analysis only cells that had ≥100 spike shuffles with the same number of detected fields (±3) as in the real data (see 'Shuffling procedures' below). Taking together all these criteria, the pool of 125 cells narrowed down to 78 cells with valid fields.

Shuffling procedures

We performed two types of shuffling to assess the significance of 3D grid cells, and in particular to assess the significance of a low CV of the inter-field distance distribution for each neuron. In the first type of shuffling ('spike shuffling': see below), we shifted rigidly the entire spike train in time, with a random circular shift for each shuffle; this method decoupled spikes from their spatial position but preserved the cell's temporal firing pattern. In the second type of shuffling ('field shuffling': see below) we moved randomly the field positions within the 3D volume covered by the bat; this method was used both as another shuffling method for validating 3D grid cells, and also as a control for the pairwise-interactions model in our theoretical work.

Spike shuffling. To assess significance, we performed per-cell shuffling of the data. The in-flight spike train was shifted rigidly and randomly by >10 s in time across the in-flight data (wrapping circularly to the beginning): this decoupled the spikes from their original spatial positions. We created 2,000 such random shuffles for each of the recorded cells, and a firing-rate map was computed for each of these shuffles, as done for the recorded data. The shuffle's firing-rate maps then underwent field detection using the same analysis pipeline as for the recorded cells. The significance of 3D grid cells (see next section) was computed using a threshold of the 95th percentile of the shuffles, taking only shuffles that had the same number of fields as in the actual neuron (±3 fields)—allowing us to compare the CV between the real data and the shuffles (see next sections).

Field shuffling. We generated per-neuron Poisson shuffling of field positions, with each shuffle having the same number of fields as the neuron; the field positions were drawn from a random uniform distribution, but were restricted to the regions within the room that were well-sampled by the bat during the recording session of the neuron ('valid region'—the coloured region in the firing-rate map of the cell). A specific shuffle (specific field arrangement) was used only if the minimal distance between all pairs of fields was >0.6 m, which is the minimal distance used in the identification of field locations from the neuronal data (see above).

Classification and analysis of multifield cells and 3D grid cells

Defining multifield cells. We classified cells with ≥10 valid stable fields as 'multifield cells'. Of the 125 recorded neurons, 66 were multifield cells. The threshold of 10 fields was chosen in order to avoid false-positive detections of an ordered lattice organization of fields, based on too few fields. In 2D, as few as three fields can produce a high gridness score; however, to show the existence of a truly repetitive lattice, one would need in principle to display at least one complete grid lattice unit—which in 2D means 7 fields (middle field + 6 neighbouring fields). Likewise, in 3D, a full unit of a close-packed lattice would require 13 fields (middle field + 12 neighbouring fields). However, in 2D it is possible to discern a true grid pattern with a smaller number of fields (as little as approximately five fields), and we therefore reasoned that one could discern a 3D lattice with approximately ten fields—but not less than that. With this in mind, only cells with at least ten fields were considered here for further analysis in search for 3D grid patterns. See Extended Data Fig. 3c for the distribution of number of fields per neuron. We note that the 10-field threshold removed 15.4% of the cells.

Behavioural non-stereotypy of fields. To ensure that fields were not formed by stereotypic flights, we conducted the following analyses. (1) To test for flight stereotypy, we examined the flight trajectories of the animal recorded for each cell, and identified the sequence of fields that each flight went through. We then asked for each recorded neuron how many flights composing the 3D map of the neuron have passed through the same sequence of fields. If there was a set of flights that passed through the same sequence of fields, it means that these flights were stereotypic. However, we show in Extended Data Fig. 4b that, in fact, the vast majority of the flights passed through a unique set of fields; that is, each flight sequence occurred only once (Extended Data Fig. 4b:

note the large peak at 1, in both histograms), which suggests that flight trajectories were not stereotypic. (2) As another way of examining flight stereotypy, we computed for each cell the percentage of fields for that cell whose underlying behavioural trajectories arrived from ≥50% of the take-off balls, or ended at ≥50% of the landing balls. We plotted the result for the population of all multifield neurons in Extended Data Fig. 5b, which showed that, for the vast majority of fields, the trajectories came from and went to many landing balls: that is, the trajectories were not stereotyped. Likewise, we examined the percentage of fields with trajectories occupying ≥50% of the direction bins; this is plotted in Extended Data Fig. 5e, showing a very high percentage of fields with broad directional coverage of the trajectories—again suggesting that the trajectories were not stereotyped. (3) To examine in yet a different way whether the flight behaviour was stereotypic, we calculated the Rayleigh vector length (RV) of the 2D (xy) projections of the trajectories passing through each field. Twenty example fields are shown in Extended Data Fig. 4c: here we plotted the xy projection of the trajectories passing through those 20 fields. We took one example field from approximately every fifth percentile of the RV distribution; the top-left example is from the first percentile (the lowest RV (most isotropic directional coverage)), and the bottom-right example is from the 99th percentile (the highest RV (most uni-directional)). The RV distribution across all fields is shown in Extended Data Fig. 4d. The distribution is strongly skewed towards low RV values, representing fields with trajectories coming from many directions. These examples and population histogram demonstrate that the trajectories passing through each field were, in the large majority of cases, non-stereotypic, and were in fact quite diverse. (4) We found that the number of trajectories through each field was very large: this could be seen from the examples in Extended Data Fig. 4c, as well as from the histograms of the number of passes through each field (Fig. 1e bottom, Extended Data Fig. 4a top), as well as the histograms of the number of passes with spikes through each field (Extended Data Fig. 4a bottom). These histograms demonstrate that each field was created by many flight passes, and by many flight passes with spikes, which supports the robustness of the fields. (5) To examine whether the neural firing inside the fields is indeed independent of the trajectory, we focused on the trajectories with spikes passing through each field and we computed from how many takeoff balls the bat took off and then passed with spikes through this field; this was also done for the landing balls (Extended Data Fig. 5c). These histograms showed that the typical fields were created by trajectories that started or ended at four or five different balls—a large number, which argues against strong effects of stereotypy. Using the same rationale, we also computed the percentage of different direction bins for trajectories with spikes that were emitted within the field (Extended Data Fig. 5f): here again, the percentage of directional bins was typically 50–70% (that is, 50–70% of all possible 360° directions)—a broad diversity of directions, which again argues against strong effects of stereotypy. We also plotted examples of individual cells, visualizing the firing rate separately for the trajectories coming from or to each specific ball (Extended Data Fig. 5a), or coming from each specific direction (Extended Data Fig. 5d). The 'checkerboard appearance' of these matrices suggests that the spikes comprising the fields originated from a diverse set of directions and a diverse set of feeder-balls, which indicates that the fields are not created by trajectories that come from specific directions or specific balls.

Field shape. To estimate the fields' shape for multifield cells, we measured the size of the field in the x, y, z directions, parallel to the room's Cartesian axes. The edges of a field were defined as the points in which the firing rate dropped below 50% of the field's peak firing-rate. We then compared the field's sizes along each of the axes, to search for population-wide elongation of fields along one of the axes – in particular, elongation in the z-dimension. We used Wilcoxon rank-sum test comparing field dimensions in x versus y, y versus z and x versus z, Bonferroni corrected for three pairwise comparisons.

Fitting FCC and HCP lattices. We created ~1.5 million versions of fields arranged in an FCC lattice and ~1.5 million versions of an HCP lattice within the flight room. We performed a brute-force search through the 7-parameter space of all possible FCC and HCP lattices, by looping over all 7 parameters that define these lattices: lattice-spacing (spacing ranging from 0.6 to 2.5 m, which covers (with margins) the range of spacings in the data: see Fig. 3b); the three Euler angles of the lattice (azimuth, pitch, roll); and the 3D shift or phase of the lattice (shift in x, y, z). To find the best-fitting lattice for each of our recorded cells, we compared each cell with all the different perfect lattice versions; this was done separately for FCC and HCP lattices. For each iteration, we found for each of the recorded fields the closest field in the perfect lattice (illustrated by the schematic in Extended Data Fig. 6b, red lines), and then we computed the squared distance between each recorded field and its closest synthetic field; we then summed these squared distances and computed the root, to yield the root mean squared (RMS) error of each cell for each of the 1.5 million FCCs or 1.5 million HCPs. The cell's lowest RMS error across all the 1.5 million FCC lattices was termed the 'FCC fit error', and was then compared to the FCC fit errors that were analogously computed for all the spike shuffles (that is, for each shuffle we found the minimal FCC fit error over the 1.5 million synthetic FCCs). The same was done for HCP. As before, we considered here only spike shuffles in which the same number of fields (±3) was detected as in the recorded cell. By locally finding the closest synthetic field to each of the recorded fields, this method did not include a 'penalty' for holes or missing fields in the recorded cell, but rather assessed the position of the detected fields only: in other words, if the recorded neuron was a nearly perfect FCC or HCP lattice with multiple missing fields ('holes'), it would still come out as a highly significant FCC or HCP.

Searching for local FCC or HCP domains. We used the 3D visualization tool OVITO[37] (Open Visualization Tool, version 3.4.3) to search for local FCC and local HCP domains in each of the multifield neurons. We treated fields as particles, imported the 3D structure of each neuron's fields into OVITO, and investigated each neuron using the 'polyhedral template matching tool'[38] available in OVITO. This tool calculates whether each particle (field) individually is arranged in a local lattice arrangement (either FCC or HCP) with respect to its nearest neighbouring fields—that is, whether it forms a local FCC or local HCP crystalline domain.

Defining 3D grid cells using CV of distances. To search for fixed distances between neighbouring fields, we computed the distance between each field and its three nearest neighbouring fields, while avoiding double counting (see Extended Data Fig. 6e for an explanation of why we took the three nearest-neighbours and not one, two or more than three). We defined two measures of a structured arrangement. (i) A global measure, to quantify the variability in the distances between fields. For each cell, we plotted the distribution of inter-field distances of all fields with their three nearest neighbours, pooled over all the fields (as in Fig. 2d). To quantify the relative width of each distribution, we computed the CV (= s.d./mean) of this distribution of inter-field distances for the cell; a low CV signifies rather fixed distances with low variability. (ii) A local measure, to account for the possibility that the fields are ordered with fixed distances locally, but these distances change across the room. To this end, we computed separately for each field the local CV of the distances between the field and its three nearest neighbours, and averaged the CV values over all fields, to obtain the cell's 'local CV'. '3D grid cells' were defined as multifield neurons that had a significant fixed-distance arrangement—that is, the CV of the cell (either global or local CV) was significantly lower than for shuffled data generated for the same cell (95th percentile shuffling; see 'Shuffling procedures' above). For this analysis, when we used spike shuffling, we considered only shuffles that yielded a similar number of fields to the actual neuron (±3 fields) and used the exact same analysis pipeline as for the real neuron; when we used field shuffling, the number of fields in each shuffle was always identical to that in the real neuron (see 'Shuffling procedures' above).

Local angles. To study the distribution of local angles between neighbouring fields (Extended Data Fig. 6c), we computed the 3D angles between each field and every pair of its three nearest-neighbours—that is, three angles for each field. To avoid angles that are created by edge effects of the room's geometry, we excluded from this analysis fields that were on the convex hull of the field arrangement (but their neighbours were allowed to be on the convex hull). We performed this analysis on both 3D grid cells and non-grid multifield cells, and compared the distribution of angles to that of shuffled data (Extended Data Fig. 6c).

'Un-distorting' the field arrangements. To examine whether the recorded 3D grid cells and non-grid multifield cells might be a distorted version of globally ordered lattices, we 'un-distorted' the field arrangements in a number of ways (see below), and then computed the CV of distances between neighbouring fields on these un-distorted field arrangements. The un-distortions were as follows:

(i) Un-scaling: shrinking or expanding the field arrangement along a cardinal axis of the room. When un-scaling along an axis, each field's distance from the middle of the room was scaled along that axis by a factor α. We calculated possible un-scaling in two axes simultaneously. For example, for un-scaling along the x and y axes (Extended Data Fig. 7a top) we show the average CV for all possible α_1 (where α_1 corresponds to unscaling along the axis denoted first: x) and all possible α_2 (where α_2 corresponds to unscaling along the axis denoted second: y). The following transformations were applied to the positions of the fields, normalized to the centre of the room:

$$T_{xy} = \begin{pmatrix} \alpha_1,\ 0,\ 0 \\ 0,\ \alpha_2,\ 0 \\ 0, 0,\ 1 \end{pmatrix},\ T_{yz} = \begin{pmatrix} 1,\ 0,\ 0 \\ 0,\ \alpha_1,\ 0 \\ 0, 0, \alpha_2 \end{pmatrix},\ T_{xz} = \begin{pmatrix} \alpha_1,\ 0,\ 0 \\ 0,\ 1,\ 0 \\ 0, 0,\ \alpha_2 \end{pmatrix}$$

We chose possible factors α (α_1 and α_2) across a range running from $\alpha = 0.33$ (shrinking the field arrangement along the axis to 1/3 of the original) and up to $\alpha = 3$ (expanding the field arrangement by a factor of 3). $\alpha = 1$ corresponds to the original field arrangement, with no change. See Fig. 2g (top left) for one example, and see Extended Data Fig. 7a for full plots of CV versus α_1 and α_2 for all the possible combinations of un-scaling (along axes xy, yz, and xz), shown for each individual bat separately, as well as for the data from all the bats pooled together.

(ii) Un-shearing: here we wanted to correct for possible shearing of fields due to walls, as described previously[4]. (the terminology 'shearing' versus 'un-shearing' is a matter of interpretation: this distortion can be called shearing if applied to a perfect lattice and un-shearing if applied to a supposedly sheared structure, to regain the lattice arrangement). We applied shearing/un-shearing by the walls over the fields of each multifield neuron, and computed the consequent CV of distances between nearest neighbours. We allowed shearing of different magnitudes controlled by a factor γ (negative γ: un-shearing to one direction; positive γ: un-shearing to the opposite direction; $\gamma = 0$ corresponds to no shearing), along two possible directions simultaneously, in up to two shearing walls simultaneously. Shearing was done relative to the room centre[4]. With the assumption of up to two shearing walls, we studied all the 15 possible shearing scenarios (Fig. 2g (top-right) shows one scenario, and Extended Data Fig. 7b shows all the 15 possible scenarios, plotted for each bat separately and also for all the bats pooled together). Below is an example transform for one of these scenarios (corresponding to Extended Data Fig. 7b (top row)):

$$T_{\substack{xz\ \text{wall}\rightarrow\text{shear}\ x\ \text{coordinate by}\ \gamma 1 \\ yz\ \text{wall}\rightarrow\text{shear}\ y\ \text{coordinate by}\ \gamma 2}} = \begin{pmatrix} 1, \gamma_1, 0 \\ \gamma_2,\ 1, 0 \\ 0, 0, 1 \end{pmatrix}$$

In this example shearing, the xz wall shears along the x coordinate with a shear parameter γ_1, and the yz wall shears along the y coordinate with a shear parameter γ_2. Similar shearing/un-shearing transformations were applied to all the 15 possible combinations of coordinates and walls, as shown in Extended Data Fig. 7b.

(iii) Un-barrelling: barrelling (also known as fish-eye lens distortion) and un-barrelling (also known as pin-cushion distortion) were performed for the fields of each multifield cell, for each of the possible 2D planes of the room (xy, yz, xz). Un-barrelling corresponds to control parameter $\beta_{\text{Un-barrel}}$, barrelling to β_{Barrel}, and no barrelling to $\beta_{\text{Un-barrel}} = \beta_{\text{Barrel}} = 0$. The transformations are given by solving the following equations: $R = r \times (1 + \beta \times r^2)$, where $r = \sqrt{a^2 + b^2}$ (a and b may equal x, y or z). For unbarrelling distortion, solve for R, whereas for barrelling distortion, solve for r.

Figure 2g (bottom) shows for one scenario the plot of the CV of inter-field distances as a function of the barrelling/un-barrelling control parameter β; Extended Data Fig. 7c shows all the possible combinations of barrelling and un-barrelling (along planes xy, yz, xz), shown for each individual bat and also for all the bats pooled together.

Defining head-direction cells and border cells

We searched for head-direction cells and border cells among the 125 recorded neurons that met the criteria detailed above (see section 'Spike sorting and inclusion criteria').

For head-direction cells, azimuthal head-direction tuning was computed as described[11] (1D azimuth bin size: 20°). The tuning was quantified using the Rayleigh vector length of the circular azimuthal tuning curve[11]. A neuron was defined as a significant azimuthal head-direction cell if its Rayleigh vector length was: (i) higher than 0.25; and (ii) higher than 95% of the Rayleigh vector lengths for shuffled data for that neuron (see ref. [11] for details on the Rayleigh vector length; we used here the spike-shuffling method (random rigid circular shift of the spike-train), as described above). The pitch head-direction tuning of neurons was computed as described[11] (1D pitch bin size: 10°). The pitch tuning width was then computed as follows: after subtracting the baseline firing, the curve's width at 20% of the peak was calculated. This tuning width was then compared to pitch tuning widths for 2,000 shuffles for that neuron (random rigid circular spike shuffling, as above). A neuron was considered to be significantly tuned to pitch if its pitch tuning width was smaller than that of 95% of the shuffles for that neuron (see ref. [11] for more details).

Border cells were defined using 2D firing-rate maps computed separately over the xy, xz and yz planes (2D views). The 2D firing-rate maps were computed using 10 × 10-cm pixels, as described[31,32], without any adaptive smoothing. We identified in each 2D map the pixels with firing rate >30% of the peak firing rate of that map, and defined a '2D firing field' as a set of such connected pixels, which covered a contiguous area >0.25 m^2. We considered only neurons for which a 2D firing field was detected in each of the cell's 2D planes. We defined an 'elongation index' for each field in each 2D plane: elongation index = the field size along the more elongated axis divided by the field size along the less elongated axis; the elongation index was computed for all three 2D planes. The elongation index was then tested for significance by comparing it to shuffled data from the same cell, in the same 2D plane (using rigid circular spike shuffling, as described above). Significant 1D border cells were then defined as 'sausage-shaped' neurons in which: (i) two of the 2D planes (2D views) exhibited firing fields with elongation index >2, which was also significantly higher than shuffled data (>99% of the shuffles); and (ii) the third plane (2D view) exhibited a firing field that was non-elongated, and was smaller in size than in the two elongated planes, thus defining a 1D 'sausage' (Extended Data Fig. 9a (left)). Significant 2D planar border cells were defined as 'pancake-shaped' neurons in which: (i) two of the 2D planes (2D views) exhibited firing fields with elongation index >2, which was also significantly higher than shuffled data (>99% of the shuffles); and (ii) the third plane (2D view) exhibited a firing-field that was non-elongated, and was larger in size than in the two elongated planes, thus defining a 2D 'pancake' (Extended Data Fig. 9a (right)).

Theta index

We computed the theta index (TI) for all the 125 recorded cells, based on the power spectrum of the spike train autocorrelations, in a similar manner to that done in previous studies in rats and bats[8,19,39,40] (autocorrelation range ± 500 ms; 10-ms bins). The TI was defined as the ratio between the mean power within 1 Hz of each side of the peak between 5 and 11 Hz, and the mean power at all frequencies. The TI was compared to a TI threshold of TI = 5, as done previously[19].

Statistics

Unless otherwise noted, for all the pairwise comparisons we used a two-tailed (two-sided) unpaired or paired *t*-test, as appropriate, with a probability threshold of 0.05. Correlations were all based on a two-tailed Pearson's correlation coefficient. We used the two-sample Kolmogorov–Smirnov test to compare distribution shapes. To assess the significance of the various properties of the 3D firing pattern—such as its similarity to FCC or HCP lattices, or the CV of local inter-field distances—we compared the real data to shuffled data: we used two types of shuffling, spike-shuffling and field-shuffling, as detailed above. We used the binomial test to assess population-wide significance of obtaining *M* out of *N* neurons as being significant, given a per-neuron significance level (arising from the shuffle) of $P_0 = 0.05$ or $P_0 = 0.01$ (see above).

Histology

Histology was done as described previously[8]. At the end of recordings, we made electrolytic lesions (DC positive current of 30 μA, 15-s duration) to assist in the precise reconstruction of tetrode positions. The bat was then given an overdose of sodium pentobarbital and, with tetrodes left in situ, was perfused transcardially using 4% paraformaldehyde. The brain was removed and thin sagittal sections were cut at 20- or 30-μm intervals. The sections were Nissl-stained with cresyl violet and were photographed to determine the locations of tetrode tracks in MEC. We subsequently used these digital photographs to assess the distances of recorded neurons from the postrhinal (dorsal) border of MEC (Figs. 1f, 3b, Extended Data Figs. 2, 8). Histology was performed for all four bats, and all tetrode-tracks were identified in MEC; in three of the four animals we were able to identify the exact recording layer and the dorsoventral coordinate for each neuron.

Modelling grid cells via pairwise interactions between fields

The modelling work was carried out in Matlab. We modelled our data by implementing pairwise interactions between fields, using three different forms of potential (that is, energy functions) that create repulsion between nearby fields and attraction between fields that are further apart (Fig. 5a). These potentials were: (i) the Lennard–Jones potential[41]—the potential used for most of our simulations; (ii) a modified Lennard–Jones potential[23]; and (iii) difference of Gaussians (DOG) potential, which is an approximation of the Mexican hat function. See below for the mathematical forms of these three potentials. These potentials differ in their strength of repulsion relative to attraction, and in how steeply the energy rises at short inter-field distances. All of these three potentials have two free parameters: (i) r_0, the characteristic length scale of pairwise interactions, which controls the equilibrium distance between two fields; and (ii) the 'temperature' *T* of the system, which controls the noise level, determining how much a field may be displaced from its equilibrium position. Note that the potential energy function has a minimum that determines the equilibrium distance between neighbouring fields: this minimum occurs at distance r_m that equals $r_m \approx r_0 \times 1.12$ (Lennard–Jones potential; Fig. 5a, Extended Data Fig. 11b), $r_m = r_0 \times 1.5$ (modified Lennard–Jones potential), and $r_m = r_0$ (DOG potential). To fit these parameters, we performed numerical simulations where the number of fields *N* matched the data.

We compared simulations of field positions done using these pairwise interactions models to three alternative models: (i) a random Poisson model in which simulated fields were randomly distributed in the 3D space covered by the bat; (ii) a jittered FCC model; and (iii) a jittered HCP model (Fig. 5b, c). See below for more details about each of these models.

Lennard–Jones model simulations. For each neuron and each set of model parameters (r_0, *T*) we generated 100 matching Lennard–Jones simulations. Each simulation was conducted using the following procedure:

1. *N* fields (equal to the number of fields of the neuron) were initialized uniformly at random locations within the neuron's 'valid region' of space (the 3D region visited by the bat on that day).

2. Fields were picked sequentially in random order. For each field *i*, a candidate displacement was drawn from a 3D Gaussian distribution with mean 0 and standard deviation $dr = (L_x L_y L_z)^{1/3}/N$, where the *L*s are the dimensions of the room (these Monte-Carlo simulations were done using the Metropolis algorithm). This *dr* was chosen in order to keep the displacement size similar to the typical distance between neighbouring fields. The candidate displacement was rejected if it moved the field out of the valid 3D region visited by the bat. We computed the field's energy before and after the displacement. The definition of the particle's energy in the Lennard–Jones model is:

$$E_i = 4\sum_{j\neq i}^{N}\left(\left(\frac{r_0}{r_{ij}}\right)^{12} - \left(\frac{r_0}{r_{ij}}\right)^{6}\right)$$

where r_{ij} is the Euclidean distance between particles *i* and *j*. To allow only field-displacements that either decreased the energy or increased it by less than the value of the thermal fluctuations (set by the temperature *T*), a displacement was accepted only if the change in the field's energy ΔE_i was smaller than a random thermal fluctuation—meaning that, given the current simulated temperature *T*, the thermal fluctuation $e^{-\Delta Ei/T}$ was greater than a random uniform number between 0 and 1 (note that a displacement was always accepted if the energy of the final position was lower than the initial position, because $e^{-\Delta Ei/T} > 1$ for $\Delta E_i < 0$). This allows a larger displacement for higher temperatures. For $T = 0$ (Extended Data Fig. 12a, b, left), a candidate displacement was accepted only if the energy decreased.

3. Step 2 was repeated 1,000 times, unless an early stopping condition was met, wherein the changes to the configuration's energy over the previous 200 repeats of step 2 was statistically indistinguishable from 0. For $T = 0$, the potential energy continued to decrease even after a much larger number of steps, so we carried out simulations for 10^5 steps, without an early stopping condition (Extended Data Fig. 12c, d).

Simulations of other pairwise-interaction potentials. Modified Lennard–Jones and DOG simulations were carried out using the same procedure as the Lennard–Jones simulations, but with a different mathematical form of the potential.

For the modified Lennard-Jones, the energy was defined to be:

$$E_i = 4\sum_{j\neq i}^{N}\left(\left(\frac{r_0}{r_{ij}}\right)^{3} - \left(\frac{r_0}{r_{ij}}\right)^{2}\right)$$

The DOG potential is defined using a parameter *s* that controls the strength of the repulsion relative to attraction. The Lennard–Jones potential is characterized by repulsion that is much larger than attraction, so here we tried to find values of *s* at which these forces were more comparable. We found that for *s* = 10, repulsion was not strong enough, and field pairs were often found much closer to each other than seen in the data. We show here results for $s = 50$, where no such discrepancy between model and data was seen. The DOG potential is:

$$E_i = \frac{1}{M(s)} \sum_{j \neq i}^{N} \left(\exp\left(-\frac{1}{2} \left(\frac{r_{ij}}{x(s) r_0} \right)^2 \right) - \frac{1}{s} \exp\left(-\frac{1}{2s^2} \left(\frac{r_{ij}}{x(s) r_0} \right)^2 \right) \right)$$

Here $M(s)$ and $x(s)$ are normalization and scaling factors, respectively, chosen such that the energy of a pair of fields is equal to s when $r_{ij} = 0$ and is equal to its minimum, −1, when $r_{ij} = r_0$.

Fitting the length scale parameter r_0 and temperature parameter T for each potential. We considered a set of Lennard–Jones model parameters: 80 cm $\leq r_0 \leq$ 160 cm (10-cm jumps); $-2 \leq \log_{10} T \leq 10$ (jumps of 0.5 in $\log_{10} T$). Additionally, for the Lennard–Jones model only, we considered $T = 0$. We then sought to find, for each neuron, the parameter values that simultaneously provide the best fit to the data for two quantities in the simulations: (i) the average nearest-neighbour distance over three neighbours for that neuron (d_{NN}), and (ii) the coefficient of variation of these nearest-neighbour distances ($\mathrm{CV}_{\mathrm{NN}}$). One hundred simulations were conducted as described above for each neuron under each parameter combination r_0, T. We then computed the average (over 100 simulations) of d_{NN} and $\mathrm{CV}_{\mathrm{NN}}$ for each simulation, in the same way as they were computed from the data. The best-fitting parameter combination was the one for which the error ε^2 was minimal, whereby:

$$\varepsilon^2 = \left(\frac{d_{\mathrm{NN}}^{\mathrm{model}} - d_{\mathrm{NN}}^{\mathrm{data}}}{d_{\mathrm{NN}}^{\mathrm{data}}} \right)^2 + \left(\frac{\mathrm{CV}_{\mathrm{NN}}^{\mathrm{model}} - \mathrm{CV}_{\mathrm{NN}}^{\mathrm{data}}}{\mathrm{CV}_{\mathrm{NN}}^{\mathrm{data}}} \right)^2$$

Poisson model simulations. We generated per-neuron Poisson shuffling of fields, with each shuffle having the same number of fields as the neuron, and the field positions were drawn from a random uniform distribution. Random field positions were restricted to the 3D region within the room that was visited by the bat during the recording session of the neuron (termed valid region, or valid behavioural region). A simulated field arrangement was used only if the minimal distance between all pairs of fields was >0.6 m, which is the minimal distance used in the identification of field locations from the neural data.

Jittered FCC and jittered HCP model simulations. To mimic a biologically plausible implementation of FCC and HCP, we considered jittered (noisy) FCC and HCP structures. For each neuron, we generated matching FCC and HCP arrangements: similarly to the pairwise-interactions models, the parameters were chosen such that both the mean nearest neighbour distance (d_{NN}) and the CV over nearest-neighbour distances ($\mathrm{CV}_{\mathrm{NN}}$) matched the data. Specifically, we computed the positions forming an FCC or HCP lattice, with the lattice spacing set to the mean of the three nearest-neighbour distances in the data (d_{NN}). We matched the CV to the data, by jittering each FCC or HCP node in 3D by a Gaussian random number with mean = 0 and standard deviation = $\mathrm{CV}_{\mathrm{NN}} \times d_{\mathrm{NN}}/\sqrt{2}$ in each direction, ensuring that the CV of distances created by these displacements is equal to the CV of the data. We chose randomly the shift of the lattice relative to the origin (3 shift parameters) and a random angle relative to the room (3 rotation angles). We accepted an instance of jittered FCC or jittered HCP lattice only if all the final nearest-neighbour distances were >0.6 m, which is the minimal distance used to identify separate fields in the experimental data.

Radial distribution function (RDF). In order to assess the orderliness of the field arrangement—and to compare this orderliness between 2D and 3D, and between the six models (Lennard–Jones, modified Lennard–Jones, difference of Gaussians, random Poisson, jittered FCC, jittered HCP)—we computed the radial distribution function (RDF) of fields. The RDF quantifies the probability of a field being at a distance r away from another field (not necessarily its nearest neighbour). Notably, while the parameters of the pairwise-interactions models were fit to the data using quantities describing the local environment (that is, mean and CV of nearest-neighbour distances: d_{NN} and $\mathrm{CV}_{\mathrm{NN}}$), the RDF contains information about the field arrangements on all length-scales in the experimental environment—beyond the nearest neighbours. Typically, when used in physics and chemistry, the RDF is computed for arrangements of particles or molecules (here, fields) with very large N, such that edge-effects are negligible. In our data, however, N (the number of fields) was not very large. We therefore did two things, as follows. (i) Minimizing the edge effects: to minimize edge effects in the RDF—both the RDF computed for the data and the RDF computed for the simulations—we considered here only distances between pairs of fields where at least one field was not a node of the convex hull of the configuration. (ii) Pooling data across neurons: to this end, we normalized the distance between every pair of fields by the average nearest-neighbour distance (d_{NN}) for that neuron; we then pooled all the valid normalized field distances from the locally ordered neurons with CV < 0.25, and computed their probability distribution, with the normalization: $\int_0^\infty \mathrm{RDF}(r) r^2 dr = 1$. To correspond to what was done in the data, we computed the six different model RDFs in a similar process: model RDFs were computed over pooled distances from simulations matched to each of the recorded cells, under the specific model. For each model, a matched-to-cell simulation was chosen randomly for each neuron and an RDF was computed for the simulated cells (pooling separately over neurons with CV < 0.25 (Fig. 5b, c, Extended Data Fig. 10a–c) and over neurons with CV > 0.25 (Extended Data Fig. 10d, e). This process was done 1,000 times (in the pairwise-interactions simulations we generated 1,000 RDFs for each tested temperature, with a matching r_0 that minimizes the error for each neuron). The RDFs were then averaged using the normalization $\int_0^\infty \mathrm{RDF}(r) r^2 dr$ (see coloured lines in Fig. 5b). To assess the distance between the data and the simulations (Fig. 5c, Extended Data Fig. 10b, e), we computed the Kolmogorov–Smirnov statistic between the RDF of the data and the RDF of each of the simulation families; this statistic was then used as our distance index between RDFs (as this is a statistic that quantifies distances between probability functions). In these computations we used $\mathrm{RDF}(r) \times r^2$, and not $\mathrm{RDF}(r)$, as $\mathrm{RDF}(r) \times r^2$ is the true probability of finding a field in 3D at a distance r from a reference field (the multiplication by r^2 accounts for the volume of a spherical shell in 3D).

Regularity index. To compare between 3D and 2D field arrangements, we sought to quantify the order found in the field arrangements from our simulations in a manner that would be independent of the dimensionality of the room, and independent of whether a lattice exists in the configuration. To this end, we computed a 'regularity index' based on the modulation depth of the second and third peaks along the distance axis (r) of the RDF, which measures the excess probability of finding fields at a particular distance, indicating a regularity (Extended Data Fig. 11a). Specifically, we defined: Regularity Index$_i$ (RI_i) = [$\max_i$(RDF) − $\min_{i-1}$(RDF)]/$\max_i$(RDF), where $\max_i$(RDF) is the i-th maximum of the RDF along the distance axis (r), and $\min_{i-1}$(RDF) is the minimal value of the RDF between the (i − 1)-th and i-th peaks: In other words, this index measures the modulation depth of the peak = the peak-to-trough difference, normalized by the peak. The RI was then defined as the maximum between RI_2 and RI_3. If a second and/or third peak did not exist (no local peak), RI for that peak was defined to be 0.

In Extended Data Fig. 13 (top graphs of each panel), we created simulations for a range of numbers of fields, N (N = 10–50 fields) and a range of room sizes, a (a = 1–10 m; in 3D we used room size: $a \times a \times a/2$, and in 2D we used: $a \times a \times$ 10-cm high room). Here the simulations were not matched to specific neurons, and the RDFs were created from distances taken from 500 simulations for each condition. The parameters used were $r_0 = 0.5$ m or 1 m and $\log_{10}T = 0$, 0.5 or 1 (where the best fitting temperature for neurons with CV < 0.25 was $\log_{10}T = 0.5$). We plotted the regularity index as the maximum over the RI for the second and third peaks, that is, $\max(\mathrm{RI}_2, \mathrm{RI}_3)$.

We also created similar plots as a function of a and linear field density ρ_0 (Extended Data Fig. 14), where we considered linear densities ρ_0 between 0.65 and 1.35 m^{-1} for $r_0 = 1$ m (Extended Data Fig. 14b, d, f), and linear densities between 1.4 and 2.6 m^{-1} for $r_0 = 0.5$ m (Extended Data Fig. 14a, c, e). The use of the linear density allows direct comparison between 2D and 3D: the linear field density ρ_0 was defined as the square root of the field density in 2D and as the cubic root of the field density in 3D.

To eliminate edge effects in all our simulations that were not matched directly to specific recorded neurons (Fig. 5d, e, Extended Data Figs. 13, 14) we used periodic boundary conditions: that is, a field displaced outside the room was returned to the other side.

Computing non-plausible regions (red-hatched area in Extended Data Fig. 13a–f top graphs): for each room size, we computed the maximal number of fields that could fit inside the room, considering a maximum packing fraction (densest packing) and a typical experimentally reported field size. Specifically, for 3D simulations, we used the maximum packing fraction of spheres arranged in an FCC (optimal packing of spheres in 3D), which is 0.74, and a typical spherical field of 1-m diameter (as observed in our data). For 2D simulations, we used the maximum packing fraction of circles arranged in a hexagonal pattern in 2D (optimal packing of circles in 2D), which is 0.907, and a typical circular field of 20-cm diameter (as previously found[24].). This yielded the following expressions for a as function of N for the red lines in Extended Data Fig. 13a–f:

$$2\mathrm{D}: a = \sqrt{\frac{N \times \pi\ (d/2)^2}{0.907}}$$

$$3\mathrm{D}: a = \sqrt[3]{\frac{2 \times N \times \frac{4}{3}\pi\ (d/2)^3}{0.74}}$$

where d is the field diameter (the factor $2 \times N$ in the numerator in 3D comes because the room size is $a \times a \times a/2$). The hatched regions below these red lines (Extended Data Fig. 13a–f) indicate non-plausible regions with a geometrically impossibly high density.

Transition from 2D to 3D. In Fig. 5e and Extended Data Fig. 11g, we systematically varied the height of the room in small increments and computed the regularity index of the field arrangements. This was done using parameters corresponding to either 3D (Fig. 5e, left column; $r_0 = 1$ m and 5 × 5 m floor), or 2D (right column; $r_0 = 0.5$ m and 2 × 2 m floor). Simulations were done while keeping either the number of fields constant (Fig. 5e top) or the effective density ρ_{eff} constant (Fig. 5e bottom). ρ_{eff} was defined as the ratio between the Lennard–Jones interaction length-scale r_0 and the mean nearest-neighbour distance d_{NN}: $\rho_{\mathrm{eff}} = r_0/d_{\mathrm{NN}}$. We simulated over $0.7 \le \rho_{\mathrm{eff}} \le 1$, which covers the range of values of ρ_{eff} found in our data (Extended Data Fig. 11f). In Fig. 5e, the bottom panels depict $\rho_{\mathrm{eff}} = 0.9$, corresponding to the 'natural' effective density of the Lennard–Jones potential, when the fields are at their equilibrium position, that is, at the minimal energy (see Extended Data Fig. 11b). Additional values of ρ_{eff} are shown in Extended Data Fig. 11g ($\rho_{\mathrm{eff}} = 0.9$ is highlighted by a thick line in Extended Data Fig. 11g). This dimensionless quantity, ρ_{eff}, is the appropriate variable to control while the room height is varied, because it quantifies where the nearest-neighbour fields are in relation to the repulsion and attraction region of the Lennard–Jones potential. This allows direct comparison between 2D and 3D. By contrast, the absolute field density makes the comparison between 2D and 3D more complicated, because the optimal packing fraction depends on dimensionality. The nearest-neighbour distance in a given simulation is not known a priori, so we ran a large number of simulations with a range of N values, and have then split the simulations post hoc according to the effective density ρ_{eff} (see the different curves in Extended Data Fig. 11g).

Computing the gridness score in 2D. Results of Lennard–Jones simulation in 2D (see example in Fig. 5d bottom-right, and Extended Data Fig. 11c bottom) were converted into 2D firing-rate maps by convolving the field arrangement with a Gaussian kernel. The kernel had a standard deviation equal to half the characteristic nearest-neighbour distance: $(L_xL_y)^{1/2}/(2N)$. These firing-rate maps of the model were used to compute an autocorrelogram, as described[8,19] (see examples in Extended Data Fig. 11c top), which was then used to compute the 'gridness score' for each simulation. The gridness score is a standard index for assessing the degree of hexagonal 60° spatial periodicity in 2D grid cells, and was computed here as previously described[8,10,19,42,43]. First, an annulus was extracted from the spatial autocorrelogram, as follows: the outer radius of the annulus was taken as the distance to the furthest of the six peaks closest to the centre of the autocorrelogram, multiplied by 1.3; the inner radius of the annulus was used to exclude the central peak of the autocorrelogram. The annulus was then rotated in steps of 60°, and the Pearson correlation coefficient r was computed between each of the rotated maps and the original map. The gridness score was then defined as:

gridness score = min (r at 60°, r at 120°) − max (r at 30°, r at 90°, r at 150°)

See distribution of gridness scores of 2D simulations in Extended Data Fig. 11d.

Additional discussion

Our finding that 3D grid cells exhibit local order (local distances) without a global lattice stands in striking contrast to theoretical models of 3D grid cells, which predicted global hexagonal lattices in 3D[16–18]. This result could not be explained by jittered perfect lattices, nor by lattice distortions such as shearing or scaling, nor by the bats' behaviour—which was volumetric and non-stereotypic (further, even if the behaviour was stereotypic, this would probably not affect the grids, because 2D grid structure in rats is not affected by highly-stereotyped behaviour[45]). We modelled 3D grid cells using pairwise interactions between fields. In 3D, the model yielded a characteristic distance between fields, creating local order but no global lattice—as we observed in our data. In 2D, the same model yielded long-range order, often with perfect hexagonal lattices. Thus, a single model described both 3D and 2D grid cells.

A fundamental difference between 3D and 2D also arises in sphere packing problems in physics, in the phenomenon of 'jammed packing'[46]. Packed spheres confined to a 2D surface tend to form hexagonal patterns—the optimal packing solution—whereas jammed spheres in 3D exhibit local but not global order (getting stuck in a sub-optimal solution (local minimum))[46]. Thus, in both physical and neural systems, 3D packing is truly different from 2D packing.

Our model leads to a prediction for 2D grid cells in large environments. The model shows a breakdown of 2D hexagonality in an environment that is large relative to the inter-field distance (Extended Data Fig. 11e). We therefore predict that in rat grid cells recorded in very large 2D boxes, 2D grids with a scale (spacing) that is small compared to the room-size will have a disrupted hexagonality, whereas 2D grids with a large scale (large spacing) will be hexagonal.

What are the mechanistic implications of our results? While the pairwise interactions model is phenomenological, such pairwise interactions between fields may arise mechanistically from plasticity in feedforward synaptic inputs to 3D grid cells. We speculate that an interaction profile similar to our model arises from competitive spike timing dependent plasticity (STDP) or competitive STDP-like plasticity among feedforward synapses containing both Hebbian and anti-Hebbian components[25]. Indeed, several recent theoretical studies showed that plasticity mechanisms acting in synapses from CA1 place cells to MEC neurons can create effective pairwise interactions between the firing fields of grid cells[47–49].

A key question then arises: are our results consistent with an attractor mechanism for grid cells? In 2D, there is compelling evidence for low-dimensional attractor dynamics within each grid cell module[50,51]. A naive generalization of classical 2D attractor models[26,51,52] to 3D would probably yield global order in the 3D fields, which is inconsistent with our data. Therefore, existing attractor models would need to be modified substantially in order to reconcile them with our findings in 3D of local but not global order. For example: (i) one possibility is that the lack of global order in 3D arises at the level of the network bumps of activity. In 3D, the arrangement of these bumps might lose its global order, owing to a mismatch with the inputs from the hippocampus—and these network-level alterations could lead to locally but not globally ordered arrangements of firing fields for individual 3D grid cells, as seen in our data. (ii) A second possibility is that the network bumps of activity remain similarly organized in 3D and in 2D, and the lack of global order in 3D arises at the level of the association between the attractor's toroidal manifold and the animal's spatial position[53]. A distorted association could yield a local but not global order in 3D grid fields. (iii) A third possibility is that the attractor dynamics is manifested only in 2D but not in 3D. All of these possibilities entail a fundamental difference between the neuronal mechanisms for representing 2D versus 3D space.

Finally, our results have important implications for the possible functional role of grid cells in the brain. Classical theories on the function of 2D grid cells have proposed that these neurons implement an efficient coding scheme for position[1,26–30,54]. However, these theories relied on the fundamental assumption that grid cell firing patterns are periodic[28–30,55]. Moreover, suggestions that grid cells are involved in geometric computations such as goal-directed navigation[27,30,52,54] were motivated by the highly geometric, periodic representation of 2D space by grid cells. Given our findings on the absence of global periodicity in 3D, it seems less plausible that 3D grid cells are involved in general-purpose geometric computations—particularly for large spatial scales (that is, for long-distance 3D navigation). In summary, our findings suggest that global spatial periodicity is not central to the function of grid cells, which calls for the development of new models that describe the contribution of grid cells to spatial navigation in both 2D and 3D environments.

Reporting summary

Further information on research design is available in the Nature Research Reporting Summary linked to this paper.

Data availability

The data generated and analysed in the current study are available from the corresponding author on reasonable request. Source data are provided with this paper.

Code availability

The code generated for the current study is available from the corresponding author on reasonable request.

31. Sarel, A., Finkelstein, A., Las, L. & Ulanovsky, N. Vectorial representation of spatial goals in the hippocampus of bats. *Science* **355**, 176–180 (2017).
32. Omer, D. B., Maimon, S. R., Las, L. & Ulanovsky, N. Social place-cells in the bat hippocampus. *Science* **359**, 218–224 (2018).
33. Ulanovsky, N. & Moss, C. F. Hippocampal cellular and network activity in freely moving echolocating bats. *Nat. Neurosci*. **10**, 224–233 (2007).
34. Yovel, Y., Falk, B., Moss, C. F. & Ulanovsky, N. Optimal localization by pointing off axis. *Science* **327**, 701–704 (2010).
35. Skaggs, W. E., McNaughton, B. L., Wilson, M. A. & Barnes, C. A. Theta phase precession in hippocampal neuronal populations and the compression of temporal sequences. *Hippocampus* **6**, 149–172 (1996).
36. Henriksen, E. J. et al. Spatial representation along the proximodistal axis of CA1. *Neuron* **68**, 127–137 (2010).
37. Stukowski, A. Visualization and analysis of atomistic simulation data with OVITO—the Open Visualization Tool. *Model. Simul. Mater. Sci. Eng*. **18**, 015012 (2010).
38. Larsen, P. M., Schmidt, S. & Schiøtz, J. Robust structural identification via polyhedral template matching. *Model. Simul. Mater. Sci. Eng*. **24**, 055007 (2016).
39. Brandon, M. P. et al. Reduction of theta rhythm dissociates grid cell spatial periodicity from directional tuning. *Science* **332**, 595–599 (2011).
40. Koenig, J., Linder, A. N., Leutgeb, J. K. & Leutgeb, S. The spatial periodicity of grid cells is not sustained during reduced theta oscillations. *Science* **332**, 592–595 (2011).
41. Hansen, J.-P. & Verlet, L. Phase transitions of the Lennard-Jones system. *Phys. Rev*. **184**, 151–161 (1969).
42. Langston, R. F. et al. Development of the spatial representation system in the rat. *Science* **328**, 1576–1580 (2010).
43. Wills, T. J., Cacucci, F., Burgess, N. & O'Keefe, J. Development of the hippocampal cognitive map in preweanling rats. *Science* **328**, 1573–1576 (2010).
44. Eliav, T. et al. Nonoscillatory phase coding and synchronization in the bat hippocampal formation. *Cell* **175**, 1119–1130 (2018).
45. Derdikman, D. et al. Fragmentation of grid cell maps in a multicompartment environment. *Nat. Neurosci*. **12**, 1325–1332 (2009).
46. Torquato, S. & Stillinger, F. H. Jammed hard-particle packings: from Kepler to Bernal and beyond. *Rev. Mod. Phys*. **82**, 2633 (2010).
47. D'Albis, T. & Kempter, R. A single-cell spiking model for the origin of grid-cell patterns. *PLoS Comput. Biol*. **13**, e1005782 (2017).
48. Monsalve-Mercado, M. M. & Leibold, C. Hippocampal spike-timing correlations lead to hexagonal grid fields. *Phys. Rev. Lett*. **119**, 038101 (2017).
49. Weber, S. N. & Sprekeler, H. Learning place cells, grid cells and invariances with excitatory and inhibitory plasticity. *eLife* **7**, e34560 (2018).
50. Yoon, K. et al. Specific evidence of low-dimensional continuous attractor dynamics in grid cells. *Nat. Neurosci*. **16**, 1077–1084 (2013).
51. Guanella, A., Kiper, D. & Verschure, P. A model of grid cells based on a twisted torus topology. *Int. J. Neural Syst*. **17**, 231–240 (2007).
52. Fuhs, M. C. & Touretzky, D. S. A spin glass model of path integration in rat medial entorhinal cortex. *J. Neurosci*. **26**, 4266–4276 (2006).
53. Klukas, M., Lewis, M. & Fiete, I. Efficient and flexible representation of higher-dimensional cognitive variables with grid cells. *PLoS Comput. Biol*. **16**, e1007796 (2020).
54. Burak, Y. & Fiete, I. Do we understand the emergent dynamics of grid cell activity? *J. Neurosci*. **26**, 9352–9354 (2006).
55. Rowland, D. C., Roudi, Y., Moser, M.-B. & Moser, E. I. Ten years of grid cells. *Annu. Rev. Neurosci*. **39**, 19–40 (2016).

Acknowledgements We thank A. Treves for extensive discussions, A. V. M. Herz and E. Katzav for helpful suggestions; F. Stella, E. D. Karpas, T. Tamir, A. Rubin, A. Finkelstein, S. R. Maimon, S. Ray, D. Omer, S. Palgi and A. Sarel for comments on the manuscript; J.-M. Fellous for contributing to the initial stages of this project; S. Kaufman, O. Gobi and I. Shulman for bat training; A. Tuval for veterinary support; C. Ra'anan and R. Eilam for histology; M. P. Witter for advice on histological delineation of MEC borders; B. Pasmantirer and G. Ankaoua for mechanical designs; and G. Brodsky and N. David for graphics. We thank the Methods in Computational Neuroscience course at MBL, Woods Hole, where the modelling work was initiated. N.U. is the incumbent of the Barbara and Morris Levinson Professorial Chair in Brain Research. Y.B. is the incumbent of the William N. Skirball Chair in Neurophysics. This study was supported by research grants to N.U. from the European Research Council (ERC-CoG – NATURAL_BAT_NAV), Israel Science Foundation (ISF 1319/13), and Minerva Foundation, and by the André Deloro Prize for Scientific Research and the Kimmel Award for Innovative Investigation to N.U. Y.B. acknowledges support from the Israel Science Foundation (ISF 1745/18), the European Research Council (ERC-SyG – KiloNeurons), and the Gatsby Charitable Foundation. H.S. acknowledges support from the Gatsby Charitable Foundation.

Author contributions G.G, L.L. and N.U. conceived and designed the experiments. G.G. conducted the experiments, with contributions from L.L. G.G. analysed the experimental data. L.L. and N.U. guided the data analysis. J.A., Y.B. and H.S. conducted the theoretical modelling, and J.A. analysed the model results. G.G. and N.U. wrote the first draft of the manuscript, with major input from L.L. All authors participated in writing and editing of the manuscript. N.U. supervised the project.

Competing interests The authors declare no competing interests.

Additional information

Supplementary information The online version contains supplementary material available at https://doi.org/10.1038/s41586-021-03783-x.

Correspondence and requests for materials should be addressed to N.U.

Peer review information *Nature* thanks Mark Brandon, Torkel Hafting and the other, anonymous, reviewer(s) for their contribution to the peer review of this work.

Reprints and permissions information is available at http://www.nature.com/reprints.

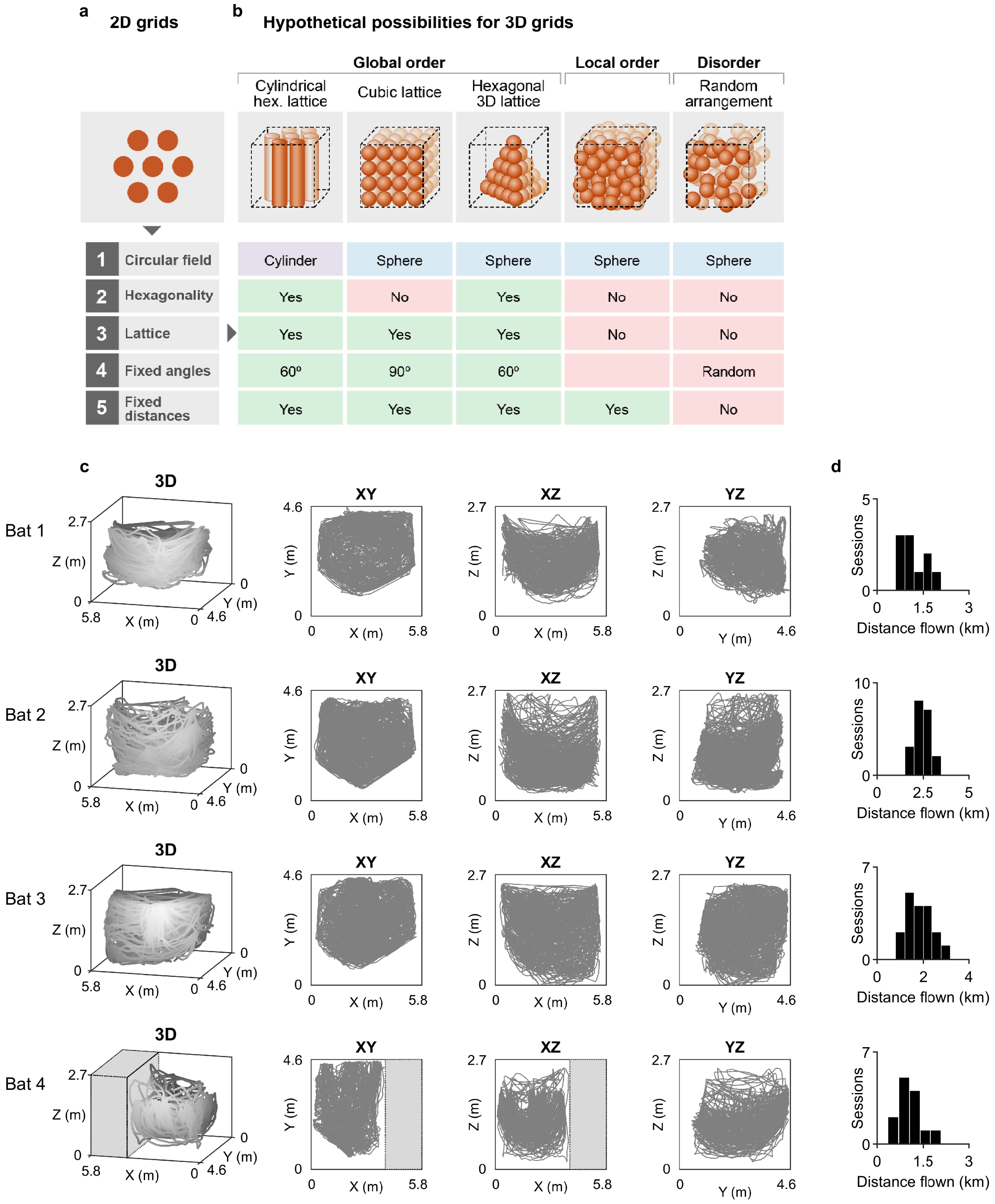

	Global order			Local order	Disorder
2D grids	Cylindrical hex. lattice	Cubic lattice	Hexagonal 3D lattice		Random arrangement
1 Circular field	Cylinder	Sphere	Sphere	Sphere	Sphere
2 Hexagonality	Yes	No	Yes	No	No
3 Lattice	Yes	Yes	Yes	No	No
4 Fixed angles	60°	90°	60°		Random
5 Fixed distances	Yes	Yes	Yes	Yes	No

Extended Data Fig. 1 | Expected properties of 3D grid cells, and coverage of 3D space by the bats' behaviour. a, Five basic properties of 2D grid cells. **b**, Expected properties of 3D grids under five hypothetical possibilities, ranging from highly ordered to random arrangement of fields. **c**, **d**, Bat behaviour covers 3D space. **c**, Examples of bat trajectories in the flight room. Rows: one example session from each of the four bats included in this study. Columns show different viewing perspectives: 3D view; top view of the room (*xy*); and side views of the room (*xz* and *yz*). Note that for bat 4 only, part of the room (grey area) was blocked off by a see-through nylon mesh (see Methods). **d**, Histograms of distance flown per session, plotted separately for each of the four bats; we included here only sessions in which we recorded at least one of the 125 well-isolated neurons that passed the inclusion criteria for analysis.

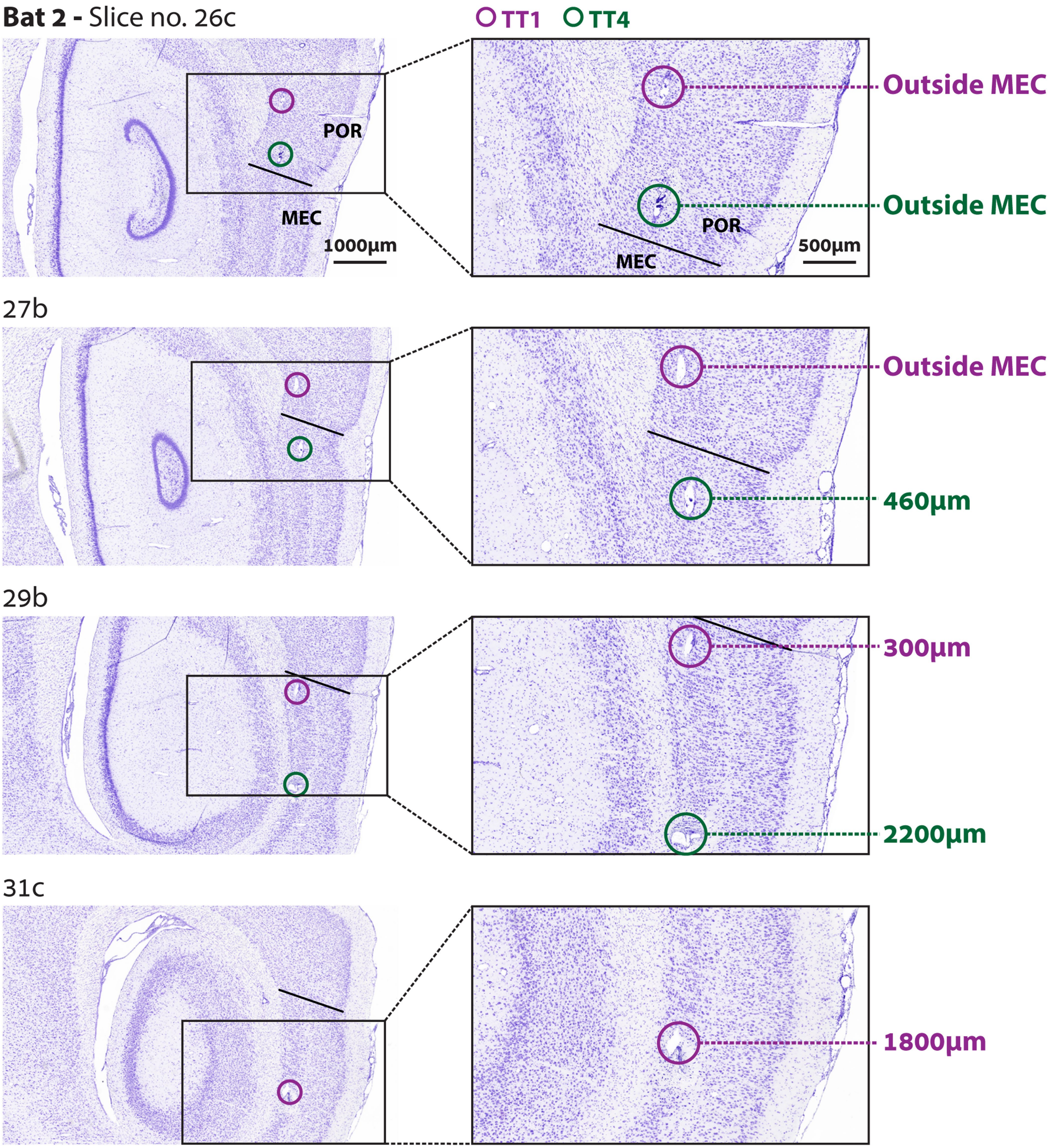

Extended Data Fig. 2 | A series of histological sections from one bat, showing two tetrode tracks in MEC layer 5. Two tetrode tracks that enter from postrhinal cortex (POR) and progress along layer 5 of MEC in bat 2. Four sagittal Nissl-stained sections are arranged from medial (top) to lateral (bottom). Left, wide view (scale bar, 1,000 µm); right, zoom-in onto the region of the tetrode tracks (scale bar, 500 µm). The postrhinal (dorsal) border of MEC is marked by a black line. The combination of the angled tetrode penetration (see Methods) and the sagittal slicing of the brain resulted in tetrode tracks that are recognizable as a small hole (sometimes surrounded by glial scar) that proceeds over many consecutive sections. The distance of the hole (track) from the postrhinal border of MEC is indicated on the right. Coloured circles mark the tracks of the two tetrodes (purple, tetrode 1 (TT1); green, tetrode 4 (TT4)). The lesion at the end of the track of tetrode 1 (purple) is visible in section 31c (section numbers are indicated). The lesion at the end of the track of tetrode 4 (green) is visible in section 29b.

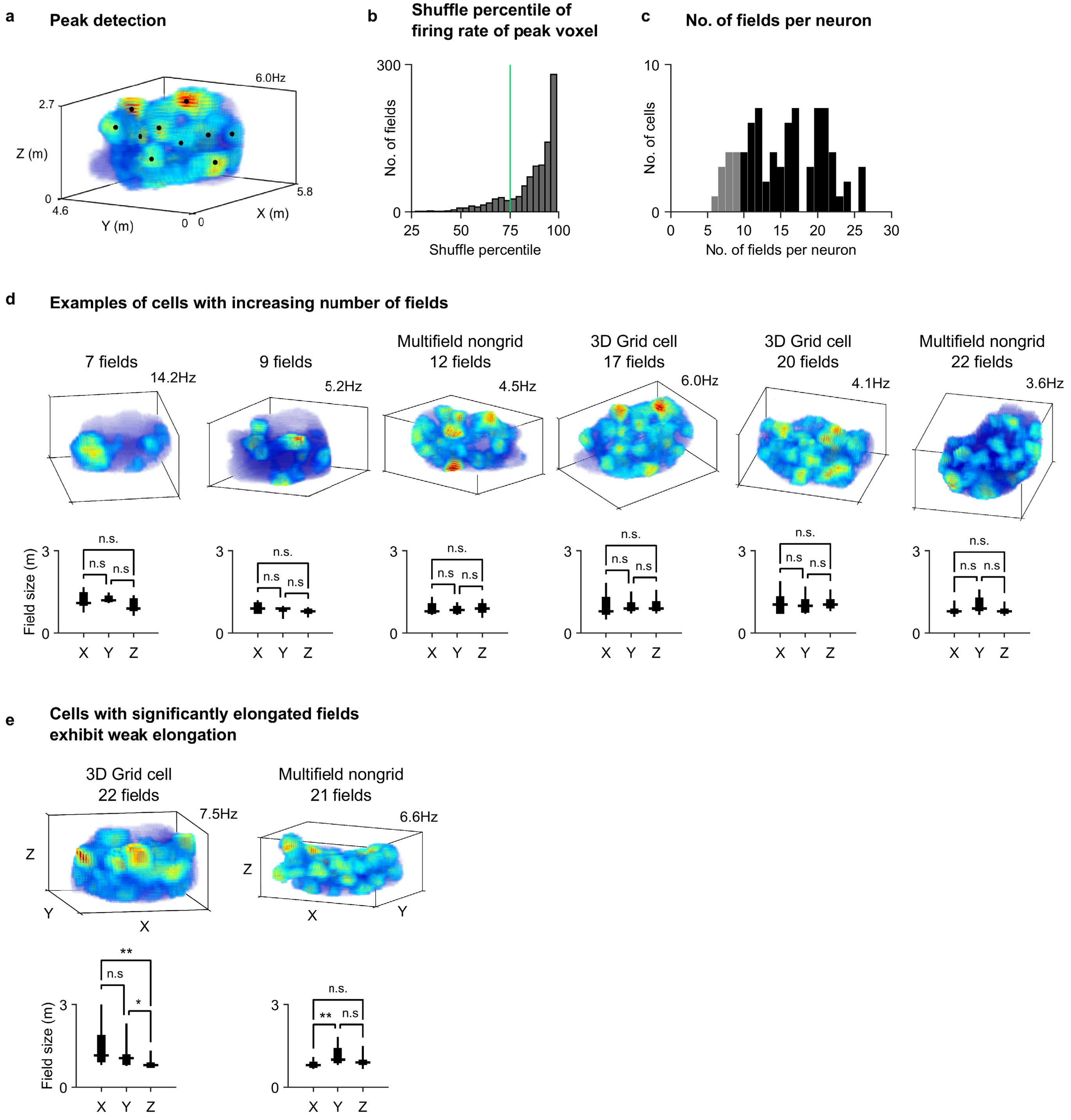

Extended Data Fig. 3 | See next page for caption.

Extended Data Fig. 3 | Firing fields, and additional examples of cells. a, Peak detection: firing-rate map of an example cell, with overlaid black dots marking the positions of the detected field peaks (see Methods). Note that only the peaks of the visible fields are displayed here (not plotting the peaks for fields 'buried' deep inside the 3D volume of the map). **b**, Threshold for peak detection shuffle (one of three criteria for a field to be valid; these three criteria narrowed the $n = 125$ cells to $n = 78$ cells): an identified peak was included in the analysis if the firing rate in its peak voxel was higher than the firing rate in the same voxel in 75% of the spike shuffles (see Methods). Shown are the shuffle percentiles for all fields (both above and below this threshold); the 75% threshold was set at a natural kink in the distribution. **c**, Number of fields per neuron: a histogram for all the neurons with valid fields ($n = 78$ cells), showing the number of fields per cell. A threshold of 10 fields was set for a neuron to be considered as 'multifield' ($n = 66$ cells, black bars; grey bars show cells below the threshold); see Methods for the rationale of setting this 10-field threshold. Example cells with varying numbers of fields are shown in **d**. **d**, Examples of cells with varying numbers of fields, including <10 fields (two left cells, not considered as multifield cells), and both grid and non-grid multifield cells with ≥10 fields. Plotted as in Fig. 2a, b. Top: 3D firing-rate maps. Bottom: box plots showing the median field sizes in the x, y and z directions. Horizontal line, median; box limits, 25th to 75th percentiles; whiskers,10th to 90th percentiles. Shown are the results of Wilcoxon rank-sum tests comparing field dimensions in x vs. y, y vs. z and x vs. z, Bonferroni-corrected for three pairwise comparisons; n.s., non-significant; the number of fields for each cell (that is, the n for each test) is written above each firing-rate map. **e**, Two example neurons with significant field elongations; plotted as in **d** (overall, 9 out of 66 neurons showed significant field elongations). Note that these two neurons differed in their elongation direction. Wilcoxon rank-sum test comparing field dimensions in x vs. y, y vs. z and x vs. z, Bonferroni-corrected for three pairwise comparisons: left cell: $P_{yz} = 0.03$, $P_{xz} = 0.003$; right cell: $P_{xy} = 0.006$ (Bonferroni-corrected for three comparisons); the number of fields for each cell (that is, the n for each test) is written above each firing-rate map. In the 9 cells with significant field elongation, fields did not resemble columns and elongation was weak and not systematic, that is, the elongation direction was heterogeneous and differed across these 9 elongated neurons.

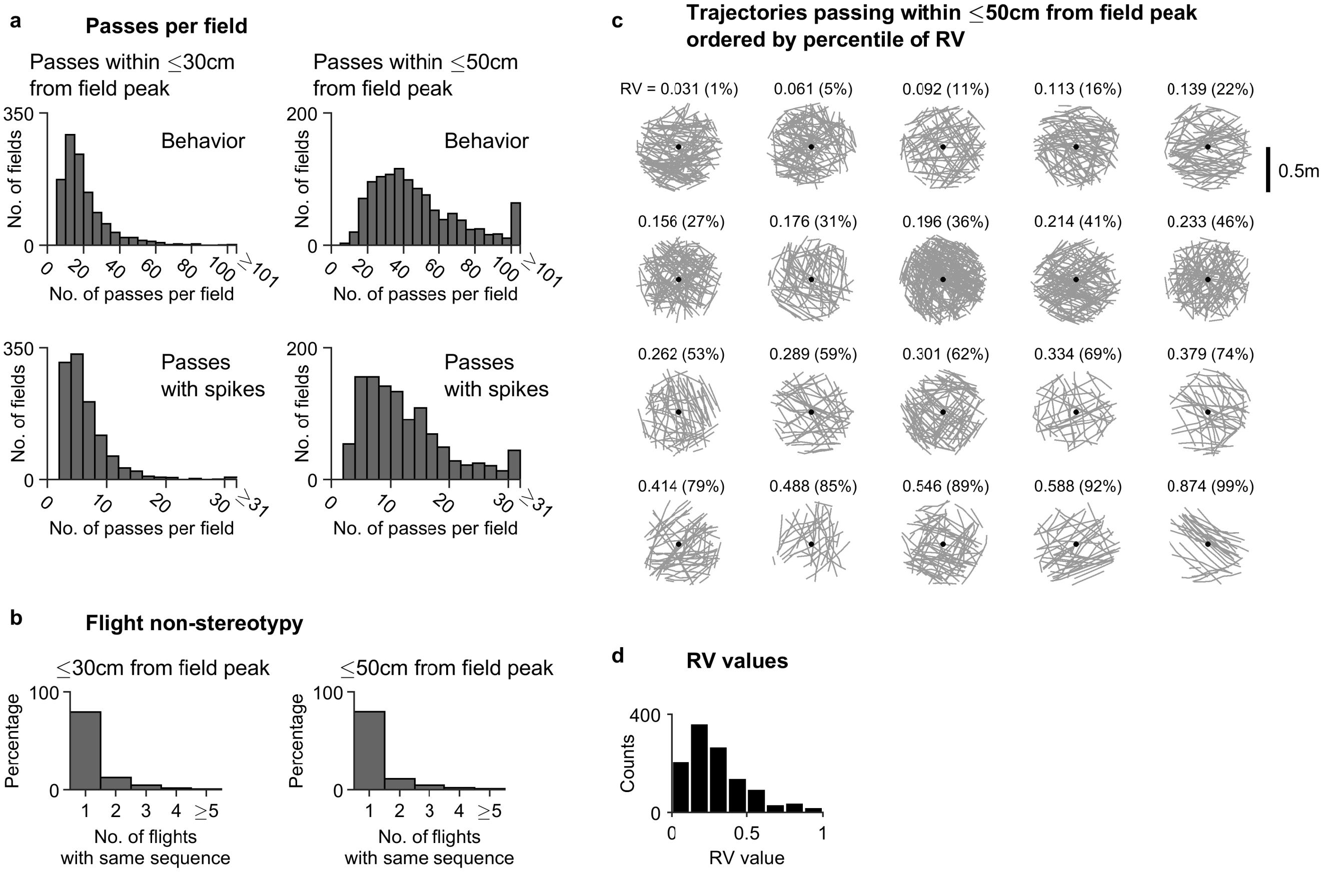

Extended Data Fig. 4 | Non-stereotypy of flights, and diversity of passes through fields: part I. a, Passes per field: histograms showing the number of flight passes creating each firing field (passes per field and passes with spikes per field serve as two of three criteria for a detected field to be considered valid). The four histograms correspond to all passes within the fields (top) and all passes with spikes within the field (bottom), computed for two different values of the radius from the field's peak: 30 cm (left) and 50 cm (right). **b**, Flight non-stereotypy: a histogram showing the percentage of flights of each cell that passed through the same sequence of fields, within two different values of the distance (radius) from the field's peak: 30 cm (left) and 50 cm (right). Flights that pass through the same sequence of fields correspond to a stereotypic trajectory of the bat: for example, if the same flight sequence repeats four times, it would appear here in the fourth bin, that is, with a value of 4 for 'No. of flights with same sequence'. The results here show that most flights are in fact unique and do not repeat more than once for the same cell (see large bin with value 1 for 'No. of flights with same sequence'), which suggests that the bats' flights were non-stereotypic. **c**, The *xy* projections of the trajectories that passed through 20 example fields. Shown are trajectories within a 0.5-m radius around the field's peak (this is the typical radius of grid fields in our data). We extracted the trajectories for all the 1,113 fields of the 66 multifield neurons, as follows: for each field we took a 3D sphere with 0.5-m radius around the field's peak, then extracted the 3D trajectories through this field, and then projected these 3D trajectories onto *xy* (2D projections). The Rayleigh vector length (RV) of the *xy*-projected trajectories was then computed for each field. Here we plotted one example field from approximately every fifth percentile of the RV distribution—a total of 20 example fields, ordered from low to high RV. The RV value and percentile (in parentheses) are indicated: top left example is from the first percentile of the RV = lowest RV (most isotropic trajectories); bottom right example is from the 99th percentile of the RV = highest RV (most uni-directional trajectories). Scale bar, 0.5 m. **d**, The RV distribution across all the fields ($n = 1{,}113$), calculated on the trajectories forming each field (see examples in **c**). Median RV of this distribution = 0.25: this is a relatively low value, indicating rather isotropic flights through most fields.

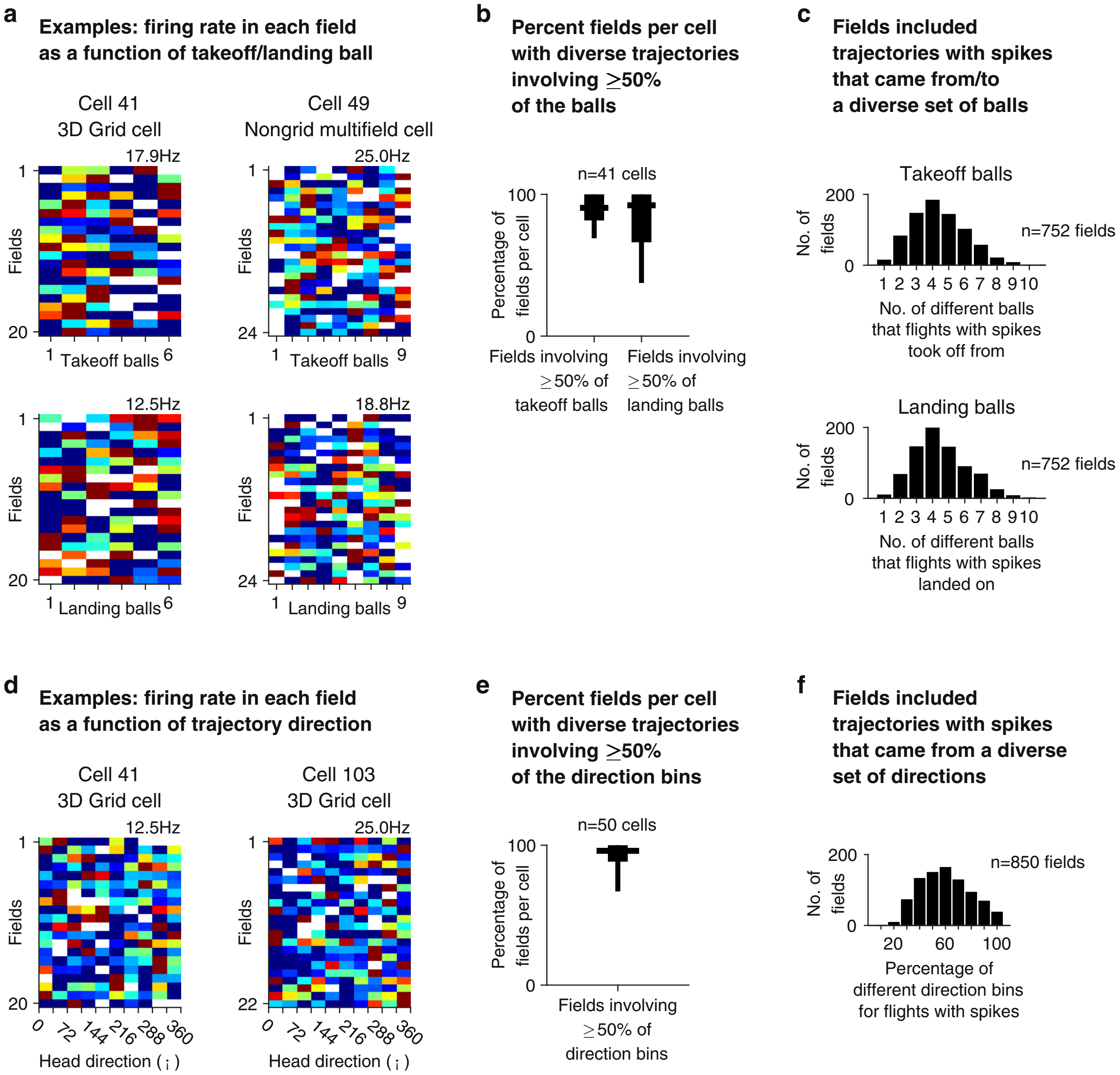

Extended Data Fig. 5 | Non-stereotypy of flights, and diversity of passes through fields: part II. **a**, Two examples of individual cells (columns), depicting the firing rates in each of the fields based on the trajectories coming from specific take-off balls (top matrices) or specific landing balls (bottom matrices); colour-coded from 0 (blue) to maximum firing rate (red; value indicated). In each matrix, the variety of firing rates in each row of the matrix (corresponding to each field) shows that the firing of each field was created by trajectories originating from a variety of take-off balls and ending on a variety of landing balls. **b**, Percentage of fields per cell that are created from diverse trajectories. Box plots show the percentages of fields per cell whose behavioural trajectories involved at least 50% of the take-off balls (left) or landing balls (right). This analysis was done for the three bats for which we used landing balls. Horizontal line, median; box limits, 25th to 75th percentiles; whiskers,10th to 90th percentiles. The high percentage shown here means that across cells, the large majority of fields per neuron involved most of the take-off balls and landing balls—that is, the bats' flights were diverse and non-stereotypic. **c**, Histograms showing the number of fields that were formed by trajectories that originated from various numbers of different take-off balls (top) and ending at various numbers of different landing balls (bottom). This analysis was done for the three bats for which we used landing-balls. **d**–**f**, As in **a**–**c**, but here instead of take-off and landing balls we examined the firing-rate at different directions of the trajectories passing through the field. This analysis was done on all the four bats. **d**, Examples of two individual cells. **e**, Percentage of fields in which the trajectories with spikes that occurred close to the field-peak (within 50 cm of the field peak) came from ≥50% of the direction bins. **f**, Distribution of the percentage of direction bins for trajectories with spikes that passed through each field. For example, 60% on the *x*-axis means that the spikes of that field came from 60% of all the possible direction bins; that is, the flight trajectories with spikes that passed through that field spanned 60% of all the possible direction bins (60% of 360°; we used here 36° bins)—a high diversity of directions.

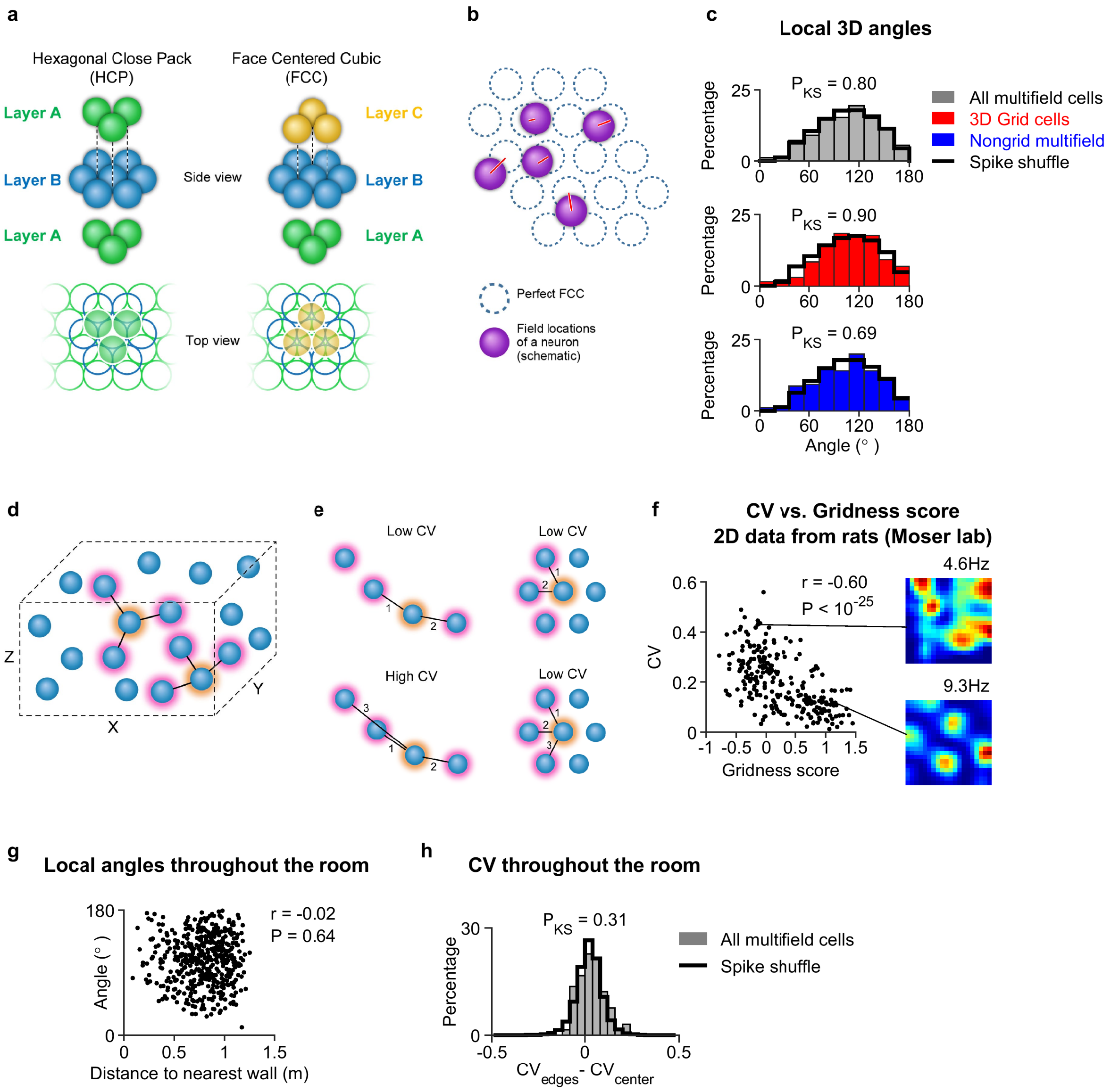

Extended Data Fig. 6 | See next page for caption.

Extended Data Fig. 6 | Searching for global and local order. a, Two lattices were proposed as theoretically probable structures of 3D grids[16,17]: these lattices exhibit a hexagonal arrangement of spheres, and were proved to be the optimal arrangement for densest sphere packing in infinite 3D space[15]. These lattice arrangements—face centred cubic (FCC) and hexagonal close pack (HCP)—are widely found in chemistry. Both of these lattices are comprised of layers of spheres arranged in a hexagonal pattern (denoted here as layers A, B and C); the two lattices differ in the phase of these layers. Each layer is placed in one of two optional sets of holes created by the lower layer: the HCP lattice has an A–B–A pattern of layers (left); the FCC lattice has an A–B–C pattern of layers (right). **b**, Illustration of the procedure of fitting data to hexagonal lattices (see Methods). Cartoon in 2D depicts the fitting that we used in 3D to fit the recorded 3D field arrangements to perfect FCC and HCP lattices. To find the best-fitting lattice for each of our recorded cells, we compared each cell with 3 million variations of FCC and HCP perfect lattices; this was done separately for FCC and HCP lattices (1.5 million variations for FCC and 1.5 million for HCP). In each iteration, we found for each of the recorded fields (purple spheres) the closest field in the perfect lattice (the simulated perfect lattice fields are depicted by dotted blue circles; red lines depict the distances between a recorded field and its nearest simulated lattice field). We then computed the squared distance from each recorded field to its closest simulated synthetic field; we summed these squared distances and computed the root, to yield the root mean square (RMS) error of each cell for each of the 1.5 million FCCs or 1.5 million HCPs. The cell's lowest RMS error across all the 1.5 million FCC lattices was termed the 'FCC fit error', and was then compared to the FCC fit errors that were analogously computed for all the shuffles (that is, for each shuffle we found the minimal FCC fit error over the 1.5 million synthetic FCC's). The same was done for HCP. **c**, Distribution of local angles. There was no angle-bias of local 3D angles, suggesting no local orientational (angular) order in the field arrangements. Top, local angles were computed between triplets of nearest-neighbouring fields; to avoid edge effects, we computed the angles only for fields that were within the convex hull of field arrangement. Grey, all recorded multifield cells; black line, shuffled data (using spike shuffling). Middle and bottom, distributions of local angles plotted separately for 3D grid cells (middle: red) and non-grid multifield cells (bottom: blue), together with shuffle data (black lines). The distributions for recorded cells did not differ significantly from the spike-shuffled data (black; indicated are the *P* values of Kolmogorov–Smirnov tests between data and shuffles). **d**, **e**, The calculation of the CV of distances to nearest neighbouring fields. **d**, Cartoon illustrating the three distances between each field and its three nearest neighbouring fields. These distances were then pooled across all fields (while avoiding double-counts), and the CV over these distances was calculated to quantify how fixed is the distance scale of the neuron (see Methods). **e**, Rationale for why the CV was computed over three nearest neighbours, and not 1, 2 or >3 nearest neighbours. Right, a perfect 2D lattice arrangement will yield low CV values regardless of how many nearest neighbours are considered: three (bottom) or two (top). Left, a periodic 1D structure ('fields along a string')—which is not a 2D lattice—may still yield a low CV when considering only two neighbours (top left), but a high CV when considering three or more nearest neighbours (bottom left). Thus, three is the minimal number of nearest neighbours that can differentiate these possibilities, and unequivocally characterize the 3D arrangement of fields. We did not use more than three neighbours, because using a large number of neighbours may accentuate possible edge effects. **f**, Comparison of the CV measure and gridness score for cells in 2D. Left, scatter plot of the CV of nearest-neighbour distances versus the classical 2D gridness score, for medial entorhinal cortex neurons recorded in rats running in 2D in the Moser laboratory (courtesy of M.-B. Moser and E. I. Moser, from https://www.ntnu.edu/kavli/research/grid-cell-data; $n = 259$ cells; we excluded from analysis putative interneurons (mean firing rate >5 Hz), non-spatial neurons (cells with spatial information <0.2 bits per spike) and border cells (manually excluded)). The Pearson correlation of this scatter and its *P* value are given in the top-right corner. Right, example firing-rate maps of two cells. Top, a spatial non-grid cell with low gridness score and high CV; bottom, a grid cell with high gridness score and low CV. The locations of these two cells on the scatter plot are indicated. Here the gridness score was computed as described in the Methods, and the CV was computed using the distances of the two nearest neighbours of each field, rather than three nearest neighbours as done for 3D cells, because in 2D many cells did not have enough fields. **g**, **h**, The lack of global order could not be explained by proximity to room borders. **g**, Local angles throughout the room: shown is a scatter plot of the local angles between triplets of neighbouring fields as a function of their distance from the nearest wall. Points were slightly jittered in the *x*-axis, for display purposes only. Pearson correlation and significance are shown. The non-significant correlation suggests that the walls did not affect the 3D arrangement of fields. **h**, CV of nearest-neighbour distances throughout the room: shown is a histogram of the differences between CVs of fields at the edges of the room and the CVs of fields in the centre of the room ($CV_{edges} - CV_{centre}$). The border between 'centre' and 'edges' of the room was defined as the median distance of all the fields from their closest wall. Grey bars, histogram for all multifield cells ($n = 66$ cells); black line, histogram for shuffles done per neuron, using spike shuffling. *P* value of Kolmogorov–Smirnov test of data versus shuffles is indicated. The non-significant difference suggests that the walls did not affect the 3D arrangement of fields.

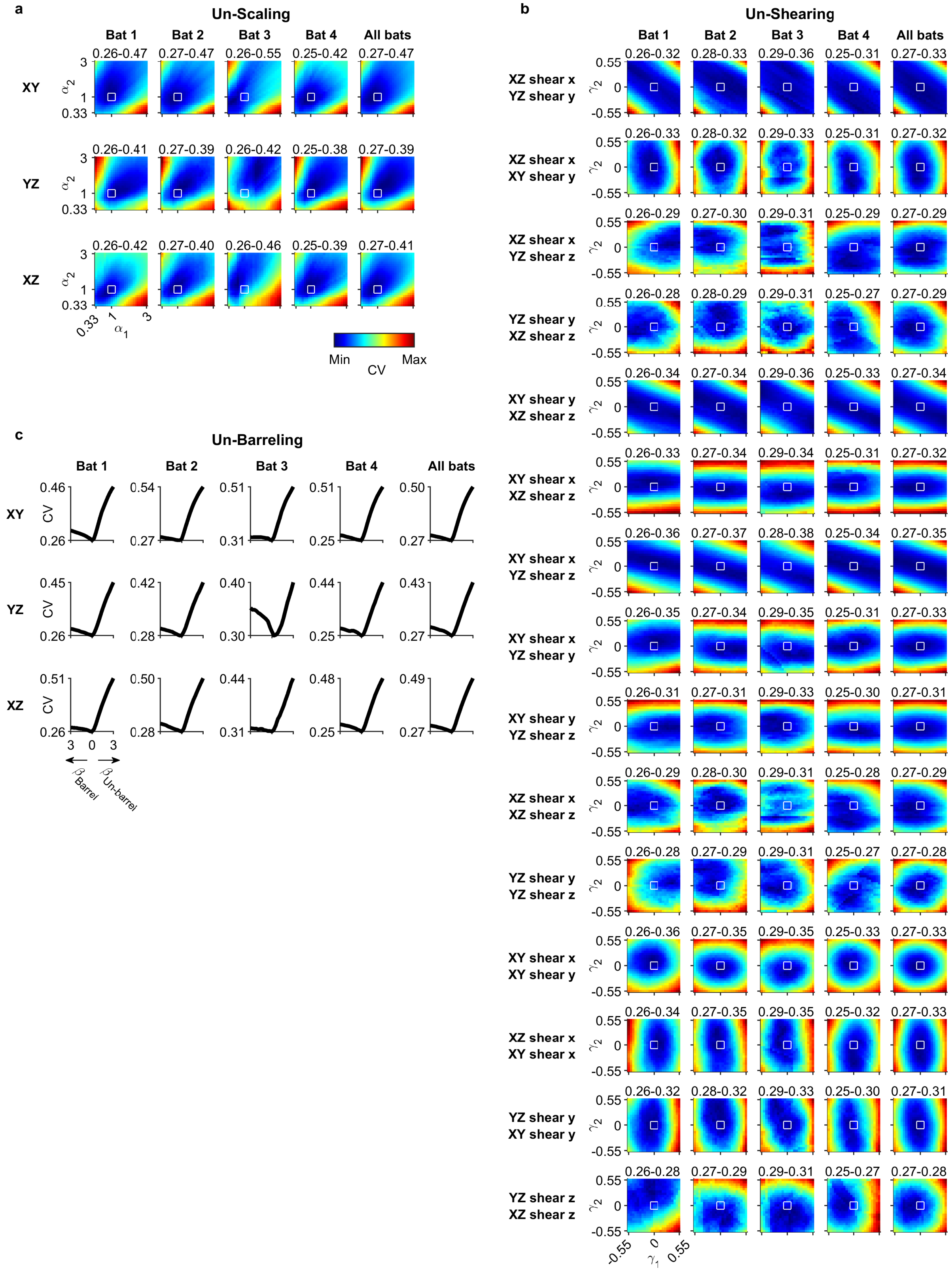

Extended Data Fig. 7 | See next page for caption.

Extended Data Fig. 7 | The firing of 3D grid cells and non-grid multifield cells cannot be explained via a global lattice that undergoes distortions (scaling, shearing, or barrelling). **a**–**c**, Mean CVs of distances between neighbouring fields, calculated after un-distorting the field positions of multifield cells ($n = 66$); shown separately for each individual bat (columns 1–4), and for all the cells from all bats pooled together (column 5). We did three types of un-distortion: un-scaling, un-shearing, and un-barrelling (see Methods). **a**, Un-scaling: field positions were scaled by a factor α along the specified axis. $\alpha < 1$ corresponds to shrinking towards the middle of the room along the specified axis, $\alpha > 1$ means expansion, $\alpha = 1$ corresponds to no change. The three rows correspond to un-scaling along three pairs of axes: *xy*, *yz*, and *xz*. Each heat-map describes the mean CV for all possible combinations of un-scaling of two axes: α_1 describes the first axis (in *xy* (first row) it corresponds to *x*), and α_2 describes the second axis (in *xy* it corresponds to *y*). CV is colour-coded from minimal value (blue) to maximal value (red), and these values are written above each matrix. White squares indicate no scaling ($\alpha_1 = \alpha_2 = 1$, that is, original data). **b**, Un-shearing: the fields of each cell underwent shearing/un-shearing as described[4] (see Methods), where shearing was done by two walls simultaneously (yielding 15 possible combinations of shearing, all shown here (rows)); we computed the two possible shearing directions (positive and negative γ-factor, which can also be thought of as shearing and un-shearing). The writing on the left indicates the two walls that create the shearing and the axes in which the shearing is occurring (for example, *xz* shear *x* means that the *xz* wall is creating a shearing along the *x*-axis). Factor γ_1 corresponds to the first line (for example, *xz* shear *x* in the top row), and γ_2 corresponds to the second line (for example, *yz* shear *y* in the top row). Heat-map shows mean values of CV, colour-coded from minimum (blue) to maximum (red; values indicated above the panel). White squares indicate no shearing ($\gamma_1 = \gamma_2 = 0$, that is, original data). **c**, Un-barrelling: a barrelling transformation (also known as fisheye lens distortion) and un-barrelling transformation (also known as pin-cushion distortion) was performed on the field arrangement of each cell. Plots show mean CV values as a function of the barrel and un-barrel factor β, for the different 2D planes along which the barrelling/un-barrelling was done (*xy*, *yz*, *xz* (rows)). All the transformations in **a**–**c** (scaling, shearing, barrelling) showed that distorting or un-distorting away from the original field arrangement increases the CV—which argues against the notion that the original field arrangements constitute a global lattice that underwent distortions.

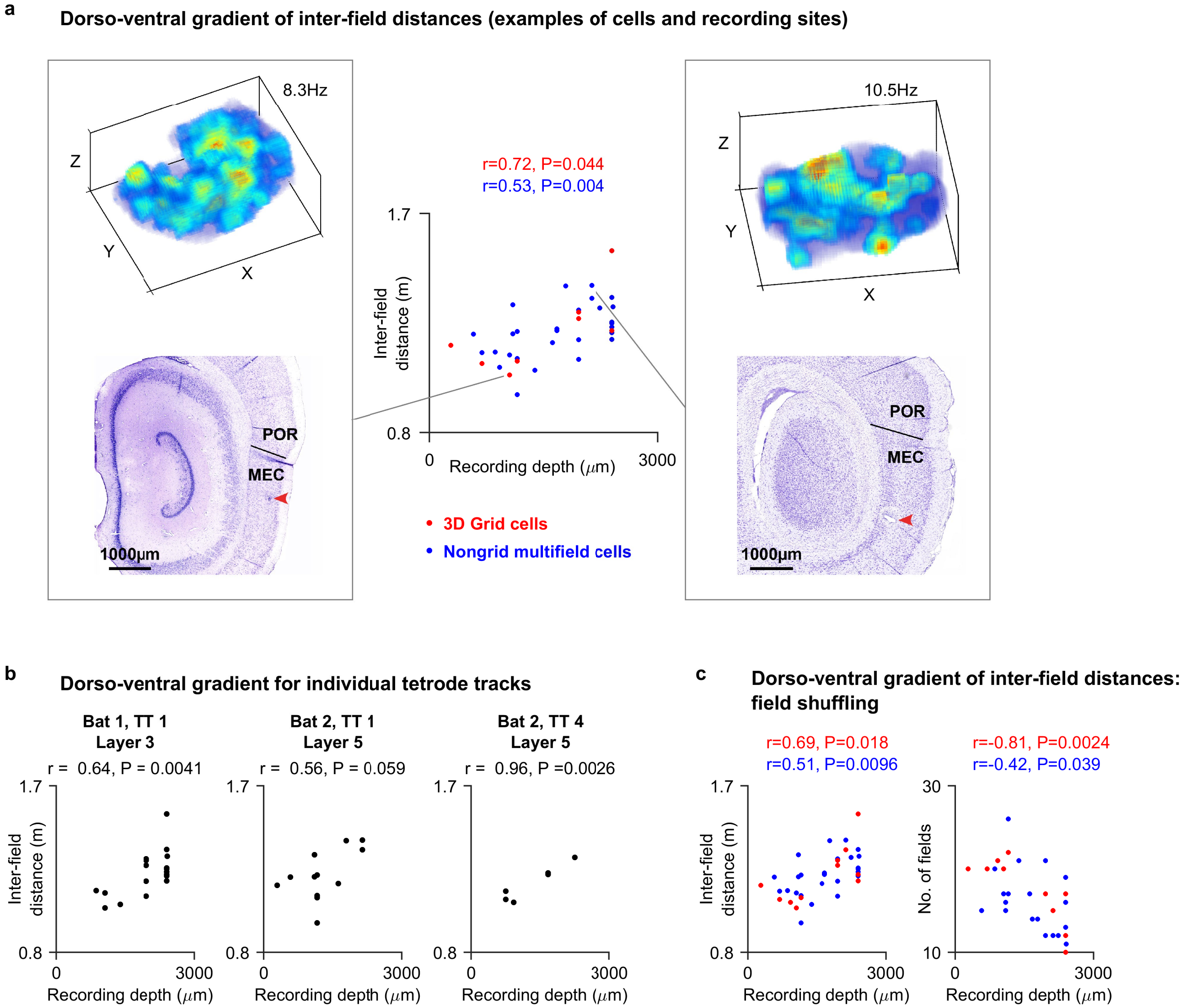

Extended Data Fig. 8 | Both 3D grid cells and non-grid multifield cells exhibit an anatomical gradient along the dorsoventral axis of MEC, as seen in rodent 2D grid cells. a, Examples of recording sites and firing-rate maps of cells along the inter-field distance gradient, here using the spike-shuffling method as in Fig. 3b. Central scatterplot: both 3D grid cells (red) and non-grid multifield cells (blue) exhibited an increase in inter-field distance as a function of the recording depth along the dorsoventral axis of MEC—akin to what is known from rodent 2D grid cells[1]. 3D grid cells were identified using spike shuffling; data points were pooled here across tetrodes and bats, and include only cells with high-quality histology that allowed precise assessment of recording depth within MEC (*n* = 8 grid cells, *n* = 28 non-grid multifield cells). Side panels: two histology examples, and their associated 3D firing-rate maps. Left, 3D grid cell recorded in layer 3; right, non-grid multifield cell recorded in layer 5. **b**, The increase in inter-field distance along the dorsoventral axis of MEC is also evident in individual tetrode tracks (TT). Shown are examples of three tetrode tracks, which proceeded mostly along a single cortical layer (indicated). Pearson correlation coefficients and their *P* values are indicated. **c**, Dorsoventral gradient, plotted as in Fig. 3b, but here classifying grid cells based on the field-shuffling method (rather than the spike-shuffling method as in Fig. 3b). We identified 20 neurons as 3D grid cells using field shuffling; included in these scatter-plots were only cells with high-quality histology that allowed precise assessment of recording depth within MEC (*n* = 11 grid cells, *n* = 25 non-grid multifield cells). Left, gradient of inter-field distances between neighbouring fields as a function of recording depth in MEC (distance from the postrhinal border of MEC); right, gradient of number of fields per cell as a function of recording depth. Note that the gradient is exhibited by both 3D grid cells (red) and non-grid multifield cells (blue), suggesting they are not two separate populations of neurons, but a continuum. Shown are Pearson correlation coefficients and their *P* values.

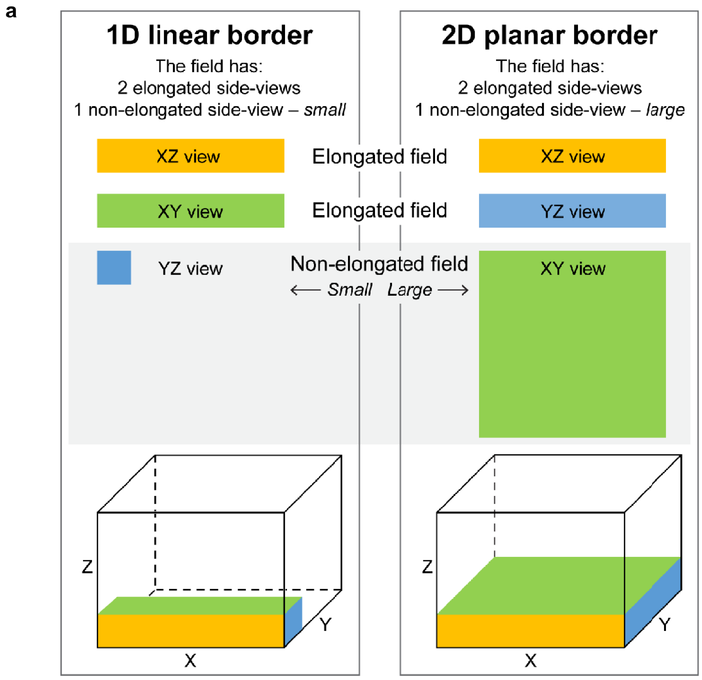

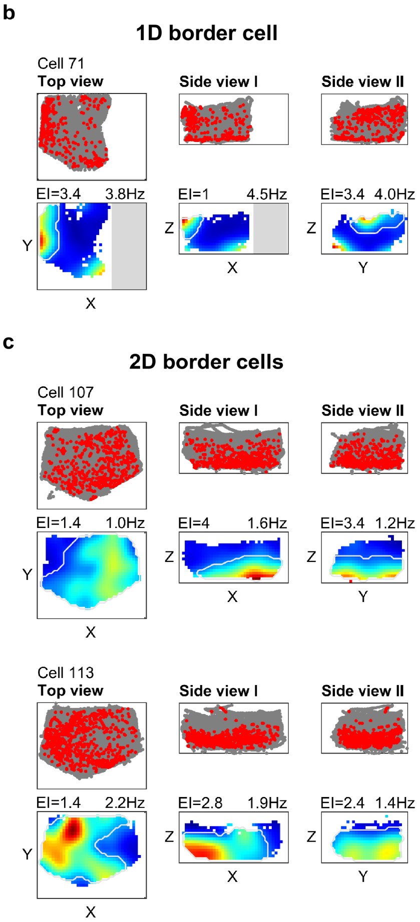

d

	Grid cells	Multifield cells	Head direction cells	Border cells
Peak FR, 3D map (Hz)	8.24±1.79	10.19±4.30	12.51±6.40	14.85±5.02
Mean FR, 3D map (Hz)	1.44±0.41	1.76±0.89	1.60±1.05	1.43±0.77
Mean FR, sp/time (Hz)	1.45±0.42	1.75±0.87	1.59±1.04	1.40±0.73
Theta index	1.99±1.27	1.32±0.95	0.81±0.48	0.75±0.37

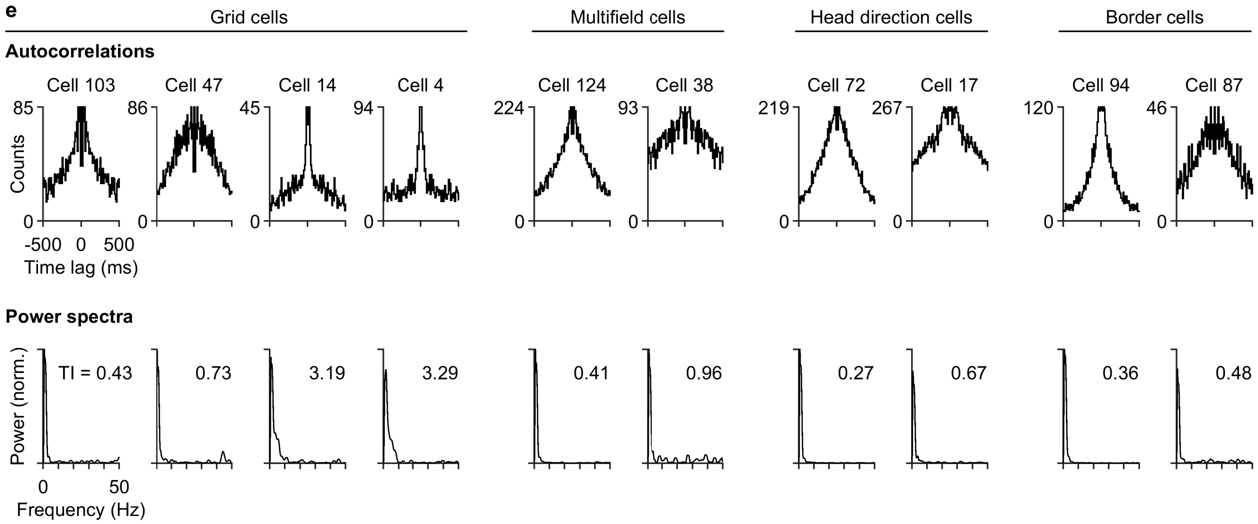

Extended Data Fig. 9 | See next page for caption.

Extended Data Fig. 9 | Border cells and firing characteristics of the various cell classes. a–**c**, Border cells. **a**, Definition of border cells in 3D arenas. We considered only neurons for which a 2D firing field was detected in each of the cell's 2D planes (see Methods). 2D firing-rate maps were plotted in the three principal 2D views of the room geometry: the top view *xy*, and the two side views *xz* and *yz* (green, orange and blue, respectively). We defined an elongation index for each field in each 2D plane as the field size along the more elongated axis/field size along the less elongated axis; the elongation index was computed separately for all three 2D planes (*xy*, *xz*, *yz*). A border field was defined as a field that was significantly elongated in exactly two out of the three views (for determining the significance we used the elongation index for each field and compared it to the elongation indices of spike shuffles; 99% criterion). Significant 1D border cells (left) were defined as 'sausage-shaped' neurons in which: (i) two of the 2D planes (2D views) exhibited firing fields with an elongation index > 2, which was also significantly higher than shuffled data (>99% of the shuffles); and (ii) the third plane (2D view) exhibited a firing field that was non-elongated, and was smaller than in the two elongated planes (left, blue square), thus defining a 1D 'sausage'. Significant 2D planar border cells (right) were defined as 'pancake-shaped' neurons in which: (i) two of the 2D planes (2D views) exhibited firing fields with elongation index >2, which was also significantly higher than shuffled data (>99% of the shuffles); and (ii) the third plane (2D view) exhibited a firing field that was non-elongated, and was larger than in the two elongated planes (right, green square), thus defining a 2D 'pancake'. **b**, **c**, A full depiction of the example border cells plotted in Fig. 4b, here shown also with trajectories and spikes, as well as an additional example. **b**, Example of a border cell that exhibited firing along a 1D border of space—in this case, along the wall edge. Left, a top view of the room (*xy*); middle, right, side views (*xz* and *yz*). Top, flight trajectory (grey) with spikes superimposed (red dots); bottom, firing rate maps, colour-coded from zero (blue) to the maximal firing rate across the three views of each cell (red). White line, edges of the detected firing field (enlarged by one bin for display purposes); indicated are the peak firing-rate and elongation index (EI; see Methods). Grey rectangle, area of the room that was made inaccessible for one of the four bats (see Methods). **c**, Examples of border cells that exhibited firing along a 2D planar border of space—in this case, the floor. Plotted as in **b**. Top cell also shown in Fig. 4b. **d**, **e**, Characteristics of the various cell classes. **d**, Firing characteristics for the different functional cell classes in MEC during 3D flight (mean ± s.d. across cells; the column of head-direction cells is based on significant azimuthal head-direction cells). Peak firing rate (FR): the highest firing rate in the 3D firing rate map. Mean firing rate: the mean of the 3D firing rate map (second row) and the ratio of total spikes in flight/total time in flight (third row); these values were very similar because the 3D behaviour was quite uniform. Fourth row: Theta index[8,19,39,40] (TI) computed as in ref. [19], where a criterion of TI > 5 was used as threshold for defining theta-modulated cells. All the cells in our study, including all the grid cells, exhibited TI < 5, indicating a lack of theta rhythmicity in the MEC of flying bats, consistent with previous findings on bat MEC cells in 2D[8,44]. **e**, Examples of spike-train autocorrelations (top) and their power spectra (bottom) for the various cell classes. The theta index is indicated above the power spectra. Note that for the four grid cells, the two leftmost examples have theta index below the population mean (see **d**), whereas the two rightmost examples have theta index above the population mean; none of these four examples exhibited clear oscillations.

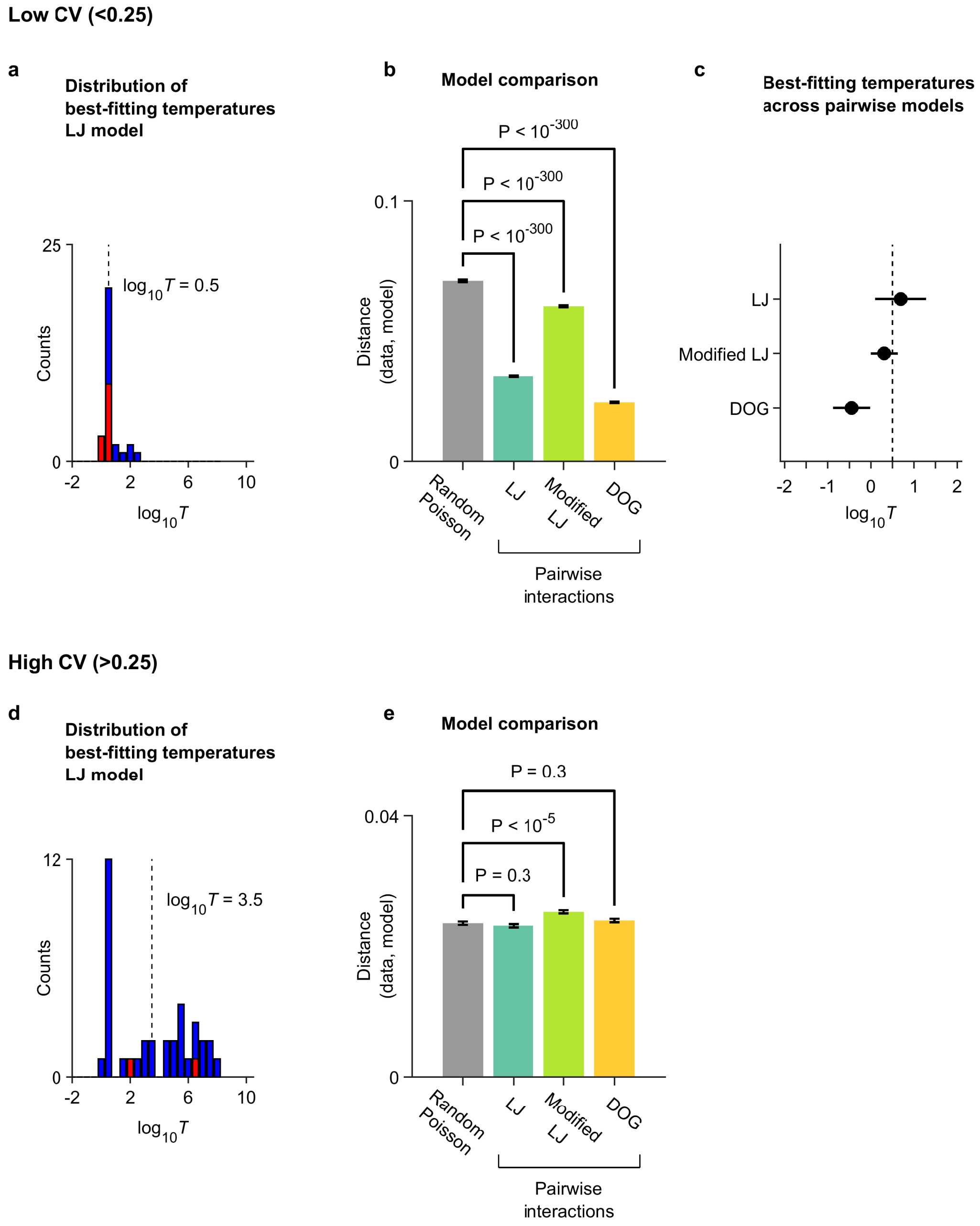

Extended Data Fig. 10 | See next page for caption.

Extended Data Fig. 10 | Distribution of best-fitting temperatures in the Lennard–Jones pairwise interactions model, and comparison to alternative pairwise-interactions models. a–**c**, Simulations of highly structured cells with low CV (CV < 0.25, *n* = 29 neurons). **a**, Distribution of the best-fitting temperatures (*T*) in the Lennard–Jones (LJ) pairwise interactions model (red, 3D grid cells identified by spike shuffling; blue, non-grid multifield cells). The best-fitting temperature for the model ($\log_{10}T = 0.5$; black dashed line) was computed as the average logarithm of the temperatures across all these cells; this temperature was consistent with the individual temperatures for almost all of the cells. The small variation in the fitted temperatures allowed us to use a single temperature for all the cells ($\log_{10}T = 0.5$, dashed line). **b**, **c**, Comparison of multiple models of short-range repulsion and long-range attraction (Lennard–Jones, modified Lennard–Jones, and difference-of-Gaussians (DOG) potentials). **b**, Quantifying the match between model and data. Three rightmost bars: distances between the RDF of the data and the RDFs of the pairwise interactions models: Lennard–Jones, modified Lennard–Jones, and DOG ($\log_{10}T = 0.5$ for all models). Left bar, distance between the RDF of the data and the RDF of the random Poisson model (in which the fields were randomly distributed in the 3D region visited by the bat). *N* = 1,000 simulated RDFs for each model; shown mean ± s.e.m. The distance between the RDFs of the model simulations and the RDF of the data was substantially smaller for the three pairwise interactions models than for the random Poisson model (*t*-test: $P < 10^{-300}$ for all three comparisons). **c**, Best-fitting temperatures (in log scale, mean ± s.d.) for neurons with CV < 0.25, plotted for the three pairwise interactions models. All these potentials yielded similar best-fitting temperatures: the Lennard–Jones and modified Lennard–Jones potentials yielded very similar best-fitting temperatures, and the DOG potential yielded a slightly lower temperature. The vertical dashed line denotes the temperature that was used for the bulk of the simulations in this study with the Lennard–Jones potential ($\log_{10}T = 0.5$). We note that for the modified Lennard–Jones and DOG potentials, the match between the RDF of the data and the RDF of the model was also very good for $\log_{10}T = 0.5$ (see **b**, where for all three pairwise interactions models we used $\log_{10}T = 0.5$). **d**, **e**, Simulations for high-CV cells (CV > 0.25, neurons not exhibiting an ordered arrangement of fields; *n* = 37 neurons). **d**, Distribution of the best-fitting temperatures in the Lennard–Jones pairwise interactions model (red, 3D grid cells; blue, non-grid multifield cells). The average logarithm of the best-fitting temperatures across these neurons was ~ $\log_{10}T = 3.5$ (black dashed line). **e**, Quantifying the match between model and data; *t*-test, *P* values indicated. Three rightmost bars: distances between the RDF of the data and the RDFs of the three pairwise interactions models (temperatures used here: Lennard–Jones, $\log_{10}T = 3.5$; modified Lennard–Jones, $\log_{10}T = 1.5$; DOG, $\log_{10}T = 1$; these were the best-fitting temperatures for each of the models; note that these temperatures correspond to a much higher noise level than in the pairwise interactions models in **a**–**c**, where we considered neurons with CV < 0.25 and fitted a temperature of $\log_{10}T = 0.5$). Left bar, distance between the RDF of the data and the RDF of the random Poisson model. *N* = 1,000 simulated RDFs for each model; shown mean ± s.e.m.

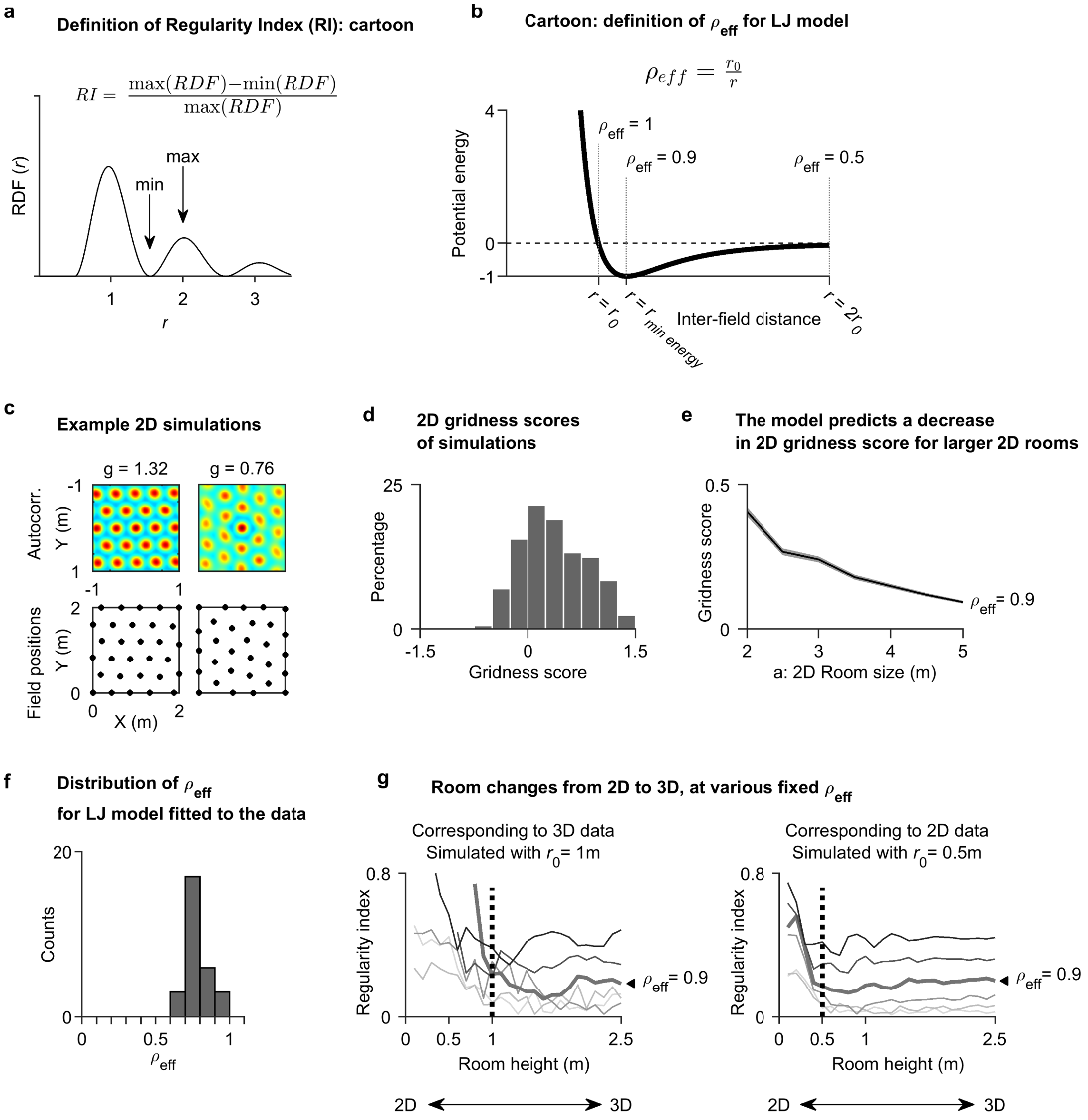

Extended Data Fig. 11 | Modelling: index definitions, 2D grids, and effective density. a, Definition of the regularity index (RI), computed as the relative height of the maximum versus the minimum in the RDF (excluding its first peak); that is, the RI reflects the modulation depth of the second (or third) peak of the RDF (see Methods). **b**, Definition of effective density ρ_{eff}, which is defined as r_0/mean inter-field distance (see Methods). Note that when the fields are at their equilibrium position, at distances equalling the minimal energy of the Lennard–Jones potential, the effective density is $\rho_{\text{eff}} = 0.9$; that is, $\rho_{\text{eff}} = 0.9$ is the 'natural' effective density. **c**, Two examples of 2D simulated cells, showing field positions (bottom) and autocorrelograms (top, zoomed in on the centre). Numbers above autocorrelograms indicate the classical 2D gridness score (*g*). The left example is also shown in Fig. 5d. **d**, Distribution of gridness scores in all the pairwise-interaction 2D simulations (room size: 2 × 2 m). Many of the 2D simulations resulted in a high gridness score, indicating a highly ordered hexagonal organization. **e**, Plot of the classical 2D gridness score[8,10,19] versus 2D room size, for our 2D model simulations (simulations in a room of size $a \times a \times 10$-cm height; the gridness score was computed as described above (see Methods) and is shown as mean ± s.e.m.; minimum 500 simulations per room size *a* (the number of simulations varied because they were chosen post hoc to match the nominal ρ_{eff})). This plot is shown for fixed effective density $\rho_{\text{eff}} = 0.9$, which is the 'natural' value for ρ_{eff}, where the local distances equal the minimal energy distance r_{min} of the Lennard–Jones potential (see **b**; note that ρ_{eff} is defined as: $\rho_{\text{eff}} = r_0/d_{\text{NN}}$, where d_{NN} is the mean nearest neighbour distance (see Methods); because $r_{\text{min}} = r_0 \times 1.12$ in the Lennard–Jones function, this yields: $\rho_{\text{eff}} = (r_{\text{min}}/1.12)/d_{\text{NN}} \approx 0.9 \times r_{\text{min}}/d_{\text{NN}}$. That is, when $d_{\text{NN}} = r_{\text{min}}$, this yields $\rho_{\text{eff}} = 0.9$). In other words, $\rho_{\text{eff}} = 0.9$ is the effective density that yields inter-field distances that match the minimum of the Lennard–Jones potential. We note that this effective density is also well within the empirically measured range of effective densities for our experimental data (see **f**). **f**, Distribution of effective density of fields ρ_{eff} in our experimental data, computed using the best-fitted scale parameter r_0 for each neuron (shown here are the $n = 29$ multifield cells with CV < 0.25). **g**, Regularity index as a function of room height. Simulations were done in 10-cm increments of room height, going from effectively 2D arena (0.1 m ceiling) to a full 3D room (2.5 m ceiling), as in Fig. 5e. Each curve was computed for a fixed effective density ρ_{eff} (see **b**); different curve shading corresponds to different ρ_{eff} values, from light to dark grey ($\rho_{\text{eff}} = 0.75$ to $\rho_{\text{eff}} = 1$). Thick curve (shown in Fig. 5e): $\rho_{\text{eff}} = 0.9$, a value within the range seen in our data (see **f**), and which is the 'natural' effective density corresponding to the equilibrium positions of the fields (see **b**). Left, computed for parameters corresponding to the 3D data, using $r_0 = 1$ m and a 5 × 5 m floor (with varying ceiling height). Right: computed for parameters corresponding to 2D data, using $r_0 = 0.5$ m and a 2 × 2 m floor (with varying ceiling height). Dashed line marks the value of r_0 used. Note the drop in regularity values when going from 2D to 3D; at this transition point the room height is slightly smaller than the distance parameter r_0 of the Lennard–Jones potential (and thus the room height allowed a second layer of fields).

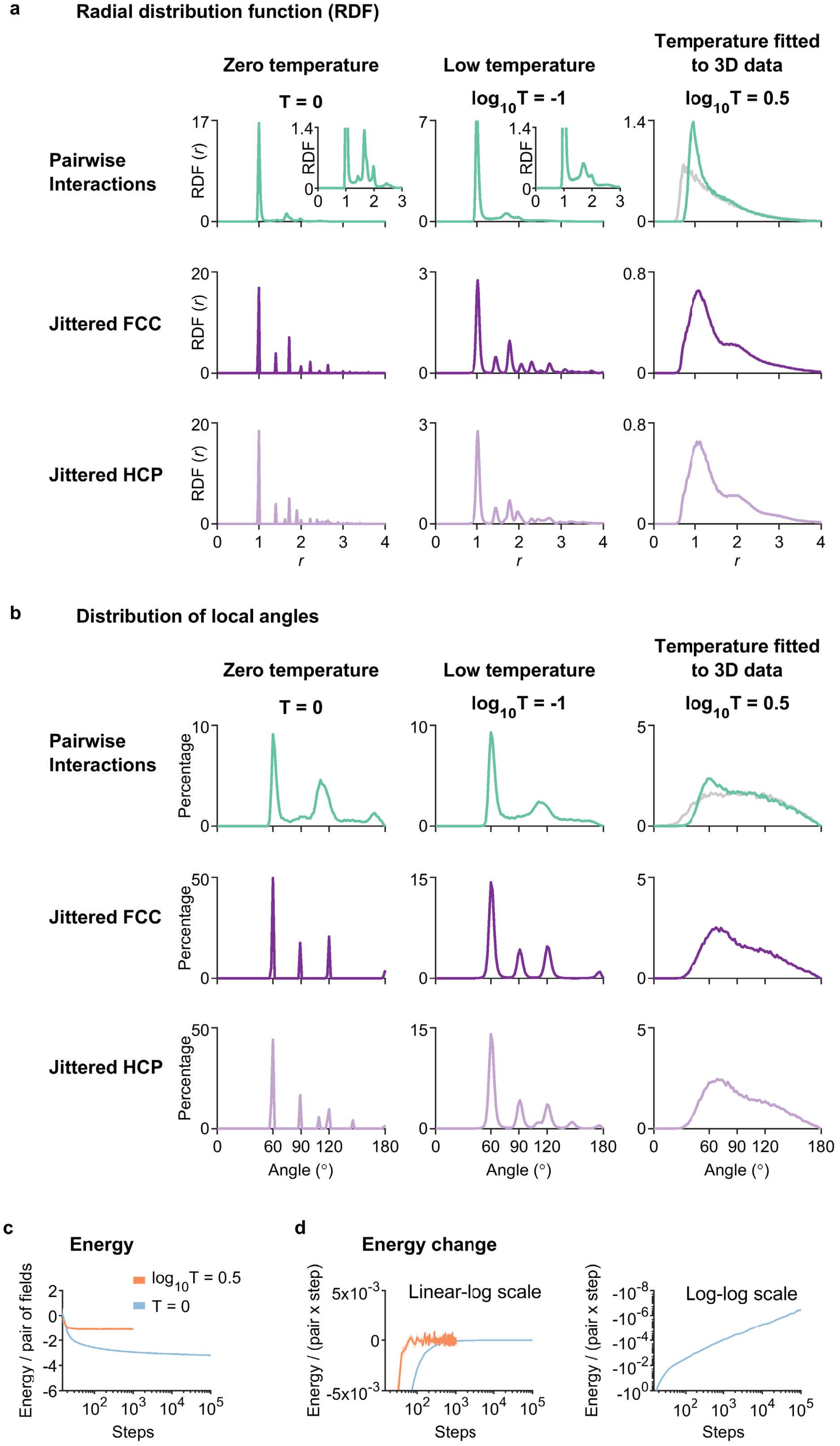

Extended Data Fig. 12 | See next page for caption.

Extended Data Fig. 12 | 3D grid cells are better explained by the pairwise interactions model than by jittered FCC or jittered HCP models; and pairwise interactions lead to a local but not global order at low temperatures of the model. a, RDF plots for three models (top row, green: Lennard–Jones pairwise interactions model; middle and bottom rows, dark and light purple: jittered FCC and jittered HCP models, where the RDFs were computed for jittered FCC and jittered HCP models with the same nearest-neighbour mean distance (d_{NN}) and CV of distances (CV_{NN}) as used in the pairwise interactions model). Each model was simulated using three temperatures (T) of the model (left, zero temperature $T = 0$, a non-biological scenario with no noise; middle, low temperature ($\log_{10}T = -1$) with little noise; right, the higher temperature that fitted well our experimental 3D data ($\log_{10}T = 0.5$)). For the temperature fitted to the data ($\log_{10}T = 0.5$), note the comparison of the RDF for the pairwise interactions model (top right, green) to the RDF for a random Poisson model (grey): the peak of the RDF is much sharper around $r = 1$ in the pairwise interactions model (green), indicating preserved local distances between nearby fields. Note that for very low temperatures with little or no jitter (left, middle), the jittered FCC and jittered HCP models showed very repetitive and distinct peaks in the RDF as a function of distance r, indicating a near-perfect lattice—as expected from FCC and HCP with no jitter ($T = 0$) or very small jitter (low temperature $\log_{10}T = -1$). By contrast, for the pairwise interactions model, at low temperatures (both at $\log_{10}T = -1$ and $T = 0$) the RDF was non-zero at all distances (see insets), which is not consistent with a perfect global lattice. At $T = 0$, the RDF seems more consistent with a distorted FCC lattice, but with preserved local distances. In other words, even at very low temperatures, the pairwise interactions model exhibited local distances without a global lattice. **b**, Distributions of local angles for the different models, following the same organization as **a**. Even at $T = 0$, the pairwise interactions model yielded field arrangements with a continuous angle distribution, with all possible angles (except very small angles that cannot occur for nearest-neighbour triangles)—in contrast to the jittered FCC and jittered HCP arrangements where angles concentrated solely in discrete values, which indicates again that even at $T = 0$, the pairwise interactions model does not exhibit a perfect global lattice. Here again, at the temperature fitted to the 3D data ($\log_{10}T = 0.5$), the pairwise interactions model yielded a more ordered arrangement than the random Poisson (top right, green curve for Lennard–Jones: see the mild peak at an angle of 60°, as compared to the grey curve for random Poisson: no peak). This means that the pairwise interactions model yielded stronger local orientational order than randomly arranged fields. **c**, **d**, Energy convergence of the Lennard–Jones pairwise interactions model at the temperature that best fitted the 3D data ($\log_{10}T = 0.5$, orange) and at $T = 0$ (light blue). **c**, Energy per pair of fields versus the step number of the simulation. **d**, Left, energy change versus the step number of the simulation, plotted in linear–log scale for both temperatures. Right, energy change of the simulations for $T = 0$, plotted in log–log scale. Shading in **c**, **d** depicts s.e.m. Note that **c**, **d** show that for the temperature which was used to fit our model to the data ($\log_{10}T = 0.5$, orange), the system converged to an asymptote very rapidly, long before we finished running the simulations—that is, the system rapidly reached equilibrium; therefore, the simulations reported in this study correspond to a system in equilibrium.

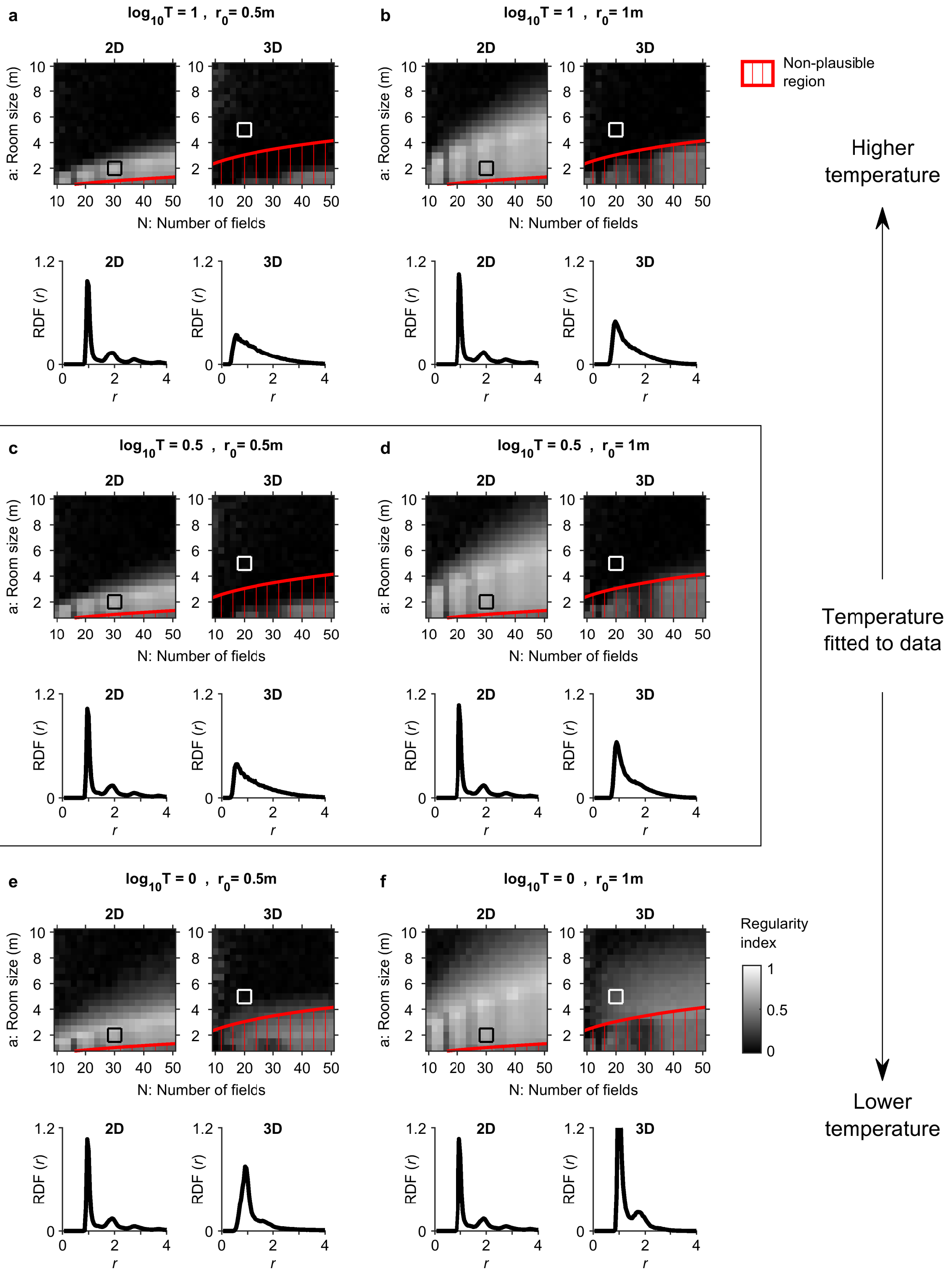

Extended Data Fig. 13 | See next page for caption.

Extended Data Fig. 13 | Comparing the pairwise interactions model for 3D versus 2D, for six combinations of model parameters T and r_0 (varying the number of fields). **a**–**f**, Regularity phase planes for 2D and 3D (see Extended Data Fig. 11a for illustration of the regularity index)—plotted as a function of room size, a, and number of fields, N. Room dimensions: 2D, $a \times a \times 10$-cm height; 3D, room-size $a \times a \times a/2$. The three rows (**a**, **b** and **c**, **d** and **e**, **f**) correspond to a changing temperature parameter T (**c**, **d** show the temperature that was best fitted to the experimental data: $\log_{10}T = 0.5$). The two columns (**a**, **c**, **e** and **b**, **d**, **f**) correspond to a changing distance parameter r_0 of the Lennard–Jones potential (values of T and r_0 are indicated). For each panel, we compared simulations in 2D (left) and in 3D (right). The top graphs in each panel show the regularity index (grey scale) for various combinations of a and N (we conducted simulations for $N \geq 10$, corresponding to multifield cells, which have ≥10 fields). Note that all these simulations exhibited much higher regularity of field arrangements in 2D than in 3D. Red hatched area denotes a non-plausible region, where the experimentally observed field diameters (~20 cm for published 2D rat grid cells[24] and ~1 m in our 3D bat grid cells) do not allow fitting N such fields into a room of size a (see Methods). The bottom graphs show the RDF as a function of r (normalized distance) for two specific values of a, N (marked by small squares in the top graphs). Left, 2D simulation for $a = 2$ m, $N = 30$ fields (the approximate arena size and number of fields for a typical rat 2D grid cell from dorsal MEC[24]); right, 3D simulation for $a = 5$ m, $N = 20$ fields (corresponding to our typical 3D data from bats). RDFs plotted as in Fig. 5d. Note that for all six parameter combinations (T, r_0; **a**–**f**), the 2D simulations showed a high regularity index (owing to a prominent second peak emerging in the RDF in 2D) for a large portion of the phase plane, and in particular in the a, N combination corresponding to a typical 2D grid cell from rat dorsal-MEC[24] (black pixel in the left panels)—whereas all 3D simulations showed a low regularity index for a, N corresponding to our data (white pixel in the right panels). A similar difference between 2D and 3D was also found when plotting phase planes of room size a versus the linear density of fields, ρ_0 (Extended Data Fig. 14).

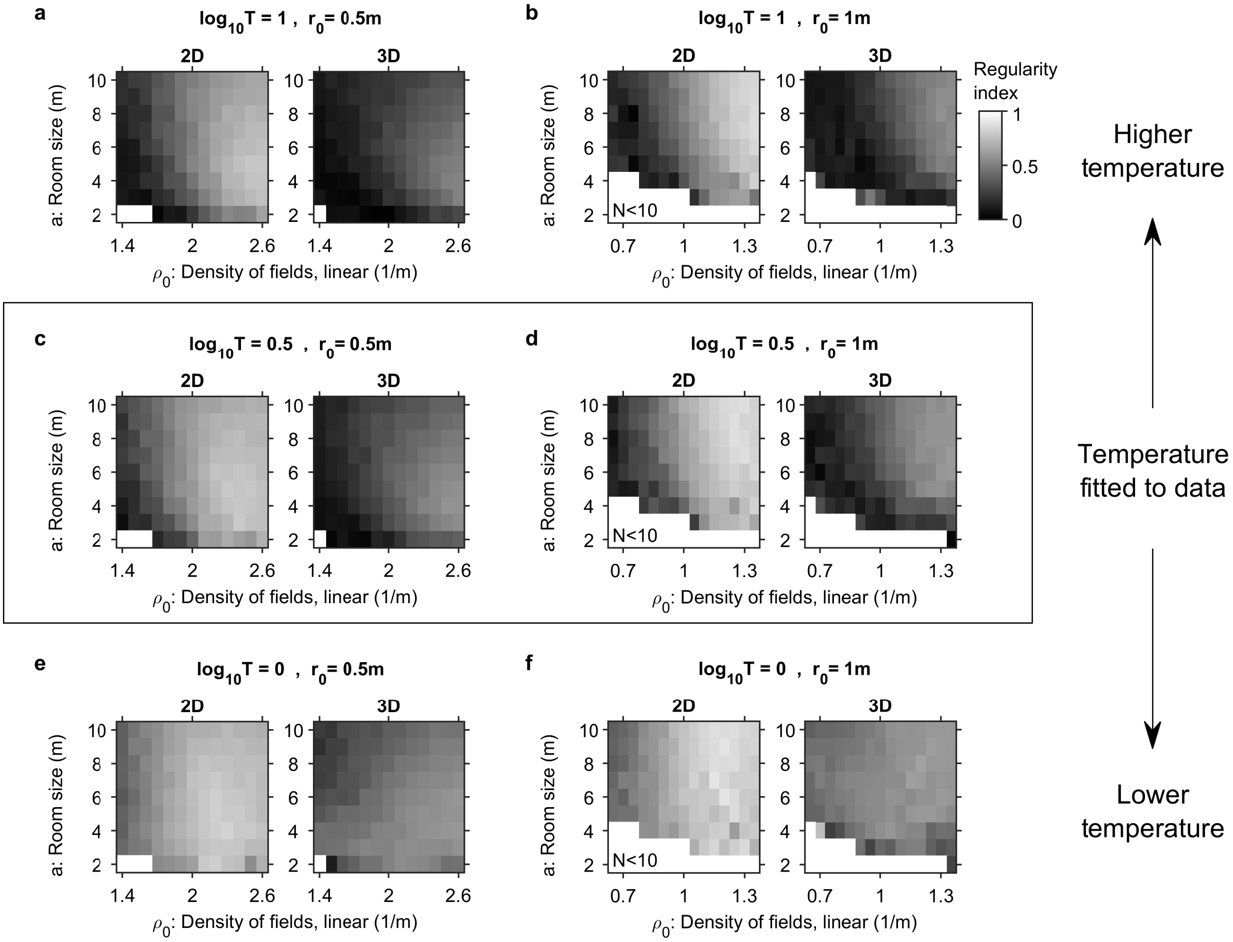

Extended Data Fig. 14 | Comparing the pairwise interactions model for 3D versus 2D, for six combinations of model parameters T and r_0 (varying the linear field density). a–f, Similar phase plane plots as in Extended Data Fig. 13, comparing 2D and 3D, where now the regularity index was plotted as a function of room size a and linear field density ρ_0 (with ρ_0 defined as the square root of the field density in 2D and cubic root of the field density in 3D). We used $r_0 = 1$ m in the right column (**b**, **d**, **f**) and $r_0 = 0.5$ m in the left column (**a**, **c**, **e**), for three temperatures T (rows; **c**, **d** show the temperature that was best fitted to the experimental data: $\log_{10}T = 0.5$). Similarly to the plots of the regularity index as a function of room size a and particle number N (Extended Data Fig. 13), these plots show the following: (i) arrangements in 2D are more ordered than in 3D (for matched density); (ii) decreasing the temperature increases the amount of order (compare the three rows); and (iii) increasing the density increases the amount of order (see monotonic dependence of the regularity index on ρ_0 within each panel).

nature research

Corresponding author(s): Nachum Ulanovsky
Last updated by author(s): June 9, 2021

Reporting Summary

Nature Research wishes to improve the reproducibility of the work that we publish. This form provides structure for consistency and transparency in reporting. For further information on Nature Research policies, see our Editorial Policies and the Editorial Policy Checklist.

Statistics

For all statistical analyses, confirm that the following items are present in the figure legend, table legend, main text, or Methods section.

n/a	Confirmed	
☐	☒	The exact sample size (*n*) for each experimental group/condition, given as a discrete number and unit of measurement
☐	☒	A statement on whether measurements were taken from distinct samples or whether the same sample was measured repeatedly
☐	☒	The statistical test(s) used AND whether they are one- or two-sided *Only common tests should be described solely by name; describe more complex techniques in the Methods section.*
☒	☐	A description of all covariates tested
☐	☒	A description of any assumptions or corrections, such as tests of normality and adjustment for multiple comparisons
☐	☒	A full description of the statistical parameters including central tendency (e.g. means) or other basic estimates (e.g. regression coefficient) AND variation (e.g. standard deviation) or associated estimates of uncertainty (e.g. confidence intervals)
☐	☒	For null hypothesis testing, the test statistic (e.g. *F*, *t*, *r*) with confidence intervals, effect sizes, degrees of freedom and *P* value noted *Give P values as exact values whenever suitable.*
☐	☒	For Bayesian analysis, information on the choice of priors and Markov chain Monte Carlo settings
☒	☐	For hierarchical and complex designs, identification of the appropriate level for tests and full reporting of outcomes
☐	☒	Estimates of effect sizes (e.g. Cohen's *d*, Pearson's *r*), indicating how they were calculated

Our web collection on statistics for biologists contains articles on many of the points above.

Software and code

Policy information about availability of computer code

Data collection	Neural data acquisition was done using a neural logger (Deuteron Technologies, SpikeLog-16). Video tracking was done using Neuralynx Cheetah (version 6.3.2). Spike sorting was done using Neuralynx SpikeSort3D (version 2.5.2.0).
Data analysis	We used custom MATLAB code for data analysis. The code generated for the current study is available from the corresponding author on reasonable request. Analysis of local lattice domain structure was done using Ovito (version 3.4.3).

For manuscripts utilizing custom algorithms or software that are central to the research but not yet described in published literature, software must be made available to editors and reviewers. We strongly encourage code deposition in a community repository (e.g. GitHub). See the Nature Research guidelines for submitting code & software for further information.

Data

Policy information about availability of data

All manuscripts must include a data availability statement. This statement should provide the following information, where applicable:

- Accession codes, unique identifiers, or web links for publicly available datasets
- A list of figures that have associated raw data
- A description of any restrictions on data availability

The data generated and analyzed in the current study are available from the corresponding author on reasonable request. Source data are provided with this paper.

Field-specific reporting

Please select the one below that is the best fit for your research. If you are not sure, read the appropriate sections before making your selection.

☒ Life sciences ☐ Behavioural & social sciences ☐ Ecological, evolutionary & environmental sciences

For a reference copy of the document with all sections, see nature.com/documents/nr-reporting-summary-flat.pdf

Life sciences study design

All studies must disclose on these points even when the disclosure is negative.

Sample size	We analyzed a dataset of 125 neurons, recorded in the medial entorhinal cortex (MEC) of 4 bats. The activity of each neuron was recorded for 1-2 hours. No power analysis was used to pre-determine the sample size: neither for the number of animals nor for the number of neurons. The numbers of animals and neurons are typical for studies in this research field.
Data exclusions	The inclusion criteria for these cells were based on sufficient behavioral coverage, spike number, and firing stability (see Methods), and are standard for this research field. Exclusion criteria were not pre-determined.
Replication	The effects described were confirmed in multiple neurons recorded over multiple recordings-sessions in 4 animals. The findings reported in this paper were found in each of the 4 individual animals.
Randomization	Not relevant, as there was no randomized treatment of the animals: This study is based on observing the neural responses to the natural behavior of the animals.
Blinding	The investigators were not blinded to the animal identity. Analysis of neural and behavior data was conducted regardless of the identity of the animal from which the data were collected.

Reporting for specific materials, systems and methods

We require information from authors about some types of materials, experimental systems and methods used in many studies. Here, indicate whether each material, system or method listed is relevant to your study. If you are not sure if a list item applies to your research, read the appropriate section before selecting a response.

Materials & experimental systems

n/a	Involved in the study	
☒	☐	Antibodies
☒	☐	Eukaryotic cell lines
☒	☐	Palaeontology and archaeology
☐	☒	Animals and other organisms
☒	☐	Human research participants
☒	☐	Clinical data
☒	☐	Dual use research of concern

Methods

n/a	Involved in the study	
☒	☐	ChIP-seq
☒	☐	Flow cytometry
☒	☐	MRI-based neuroimaging

Animals and other organisms

Policy information about studies involving animals; ARRIVE guidelines recommended for reporting animal research

Laboratory animals	Egyptian fruit bats (Rousettus aegyptiacus), wild-caught. Sex: male. Age: adult, 2-10 years of age (note: these bats live >20 years).
Wild animals	The bats in this study (4 male Egyptian fruit bats, Rousettus aegyptiacus, age: 2-10 years) were captured as adults in Israel, using butterfly nets. They were transported in a car to the Weizmann Institute, where they were quarantined and then joined a large bat colony at the Institute. After a few months in the lab, we ran the experiments described in this study. Following experiments, the bats were euthanized with Pental for purpose of brain histology.
Field-collected samples	The study did not involve samples collected from the field.
Ethics oversight	The experimental procedures described in this study were approved by the Institutional Animal Care and Use Committee (IACUC) of the Weizmann Institute of Science.

Note that full information on the approval of the study protocol must also be provided in the manuscript.